THE PENNSYLVANIA STATE UNIVERSITY
SCHREYER HONORS COLLEGE

DEPARTMENT OF MECHANICAL ENGINEERING

SCALE TIRE MODELING AND EXPERIMENTATION ON A ROLLING ROADWAY SIMULATOR

ANDREW T. GLUMAC

Spring 2006

A thesis
submitted in partial fulfillment
of the requirements
for a baccalaureate degree
in Mechanical Engineering
with honors in Mechanical Engineering

Reviewed and approved* by the following:

Sean Brennan
Assistant Professor of Mechanical Engineering
Thesis Supervisor

Domenic A. Santavicca
Professor of Mechanical Engineering
Honors Adviser

*Signatures are on file in the Schreyer Honors College.

We approve the thesis of Andrew T. Glumac:

Date of Signature

____ ______________

Sean Brennan
Assistant Professor of Mechanical Engineering
Thesis Supervisor

Date of Signature

____ ______________

Domenic A. Santavicca
Professor of Mechanical Engineering
Honors Adviser

Student ID# 983984815

ABSTRACT

The motion of a vehicle is controlled almost entirely by the forces applied to the tires by the road. For this reason, accurate modeling of tires is very important for vehicle design. Since testing on full-size vehicles is very expensive, academic vehicle dynamics testing is now often taking place on scale-sized vehicles. The goal of this project is to develop a methodology to design tires for these scale vehicles such that they have the same handling characteristics as real tires. This will allow cheaper, safer, and easier vehicle testing.

Test were performed on a 1/5 scale car on the Penn State designed rolling roadway simulator. This is essentially a large variable speed treadmill that allows a vehicle to remain in place while the roadway surface moves beneath it. The treadmill has the ability to roll side-to-side up to 25°. The vehicle is outfitted with sensors so that its yaw and steering angles can be measured. The scale car was equipped with solid rubber tires with aluminum plates on both sides, providing the ability to vary the sidewall length as well as the width of the tires. Many experiments were performed varying key components of the tire, and a linear tire model as well as Pacejka's Magic Tire model was used to evaluate the data. This analysis was performed using Excel and MATLAB. A regression analysis was performed to fit the model and to make sure that the data was statistically significant.

It was found that the cornering stiffness of the tires can be commanded to some extent through the sidewall length as well as the tire width. Sidewall length varied the cornering stiffness by about 50% in these tests. Other factors were inferred that appear affect the cornering stiffness and recommendation for further tests is given.

TABLE OF CONTENTS

ACKNOWLEDGEMENTS

The author would like to thank Dr. Sean Brennan and Vishisht Gupta for the invaluable help that they provided for this thesis.

Chapter 1

Introduction

Accurate modeling of tires is critical for vehicle design and for understanding vehicle behavior. Currently, validation of most vehicle dynamics testing takes place on full-size vehicles. This is expensive and can make certain experiments regarding safety and automation very cost prohibitive, especially for an academic institution. For this reason, scale vehicles are now tested on rolling roadway simulators, in which the vehicle remains in place and the roadway moves beneath it. The goal of this project is to develop a capability to design tires for a scale car such that they share the same handling characteristics as real tires. This will allow cheaper, safer, and easier vehicle testing on rolling roadway simulators.

The History of the Tire's Influence on Vehicle Dynamics

The study of vehicle dynamics provides the basis for designing a car that is safe and stable under all cornering, braking, and acceleration. This performance is a response to forces imposed on the vehicle and thus the study of vehicle dynamics must focus on how and why the forces are generated. The primary forces that control a vehicle are developed in four patches, each the size of a man's hand, where the tire contacts the road [1]. The ability of these tires to transmit all the forces and moments affects the vehicle's handling, comfort, and safety [2]. An intimate understanding of these forces and moments is the key to understanding vehicle dynamics [1].

In ancient Mesopotamia and northern Iran, wheeled carts are known to have been in use by about 3000 B.C. These wheels were either solid wooden disks or were formed from three planks joined together with dowels. The wooden running surfaces of the wheels on these carts had a very short life, so to overcome rim damage, leather tire coverings were attached in about 2500 B.C. Eventually, protruding copper nails which were added around 2000 B.C. By this same time wheeled vehicles were common in the Middle East and were also appearing in Europe. The Celts were the next innovators with the invention of the spoked wooden wheel. Development of carts continued with lighter, faster chariots being used for war. People began to work with iron by 1500 B.C and started to use it in vehicle bodies. Iron tires came into use around 700 B.C. Heavy pieces of iron were nailed, bolted or riveted to the outside of the wooden wheels. In about 400 B.C the Celts developed the method of shrink-fitting iron tires to a wooden frame, a practice that continued up to 1900 A.D. on wagon-wheels. This use of an iron rim was a huge advance which greatly reduced rolling resistance and simplified the production of spoked wheels. These tires were constructed by creating an iron tire that was slightly smaller than the wooden wheel, heating the iron until it expanded, and then cold shrinking it into place. These metal tires were so damaging to roads that they were banned within some cities. However, they remained a staple of transportation for many centuries and horse-drawn delivery vehicles with metal tires were still in use in many developed countries in the 1940s [3]. In addition to the damage that they caused to roads, wooden and metal tires also provided an unforgiving running surface. A more elastic material was needed for comfortable, safe and speedy travel.

Rubber appeared as a tire material in 1839 when Charles Goodyear developed a way to vulcanize it [3]. Vulcanization is a process where sulfur and heat are added to rubber to stabilize its properties. Previously the properties of rubber were too dependent on temperature, with it becoming soft and stick in warm weather and hard and brittle when it was cold [4]. By 1867 the solid rubber tire was developed enough that it was used on heavy steam locomotives that ran on highways. Solid rubber tires, however, were not a perfect solution. The high contact pressure that they exerted on the pavement significantly damaged roads and the problem came to a head after World War I. In a post-war exhibition convoy coast-to-coast across the United States, surplus US military trucks from World War 1 destroyed hundreds of miles of roads in a few weeks. The switch from solid rubber tires to pneumatic ones was recommended after a study by the Bureau of Public roads which showed that pneumatic tires could have a higher maximum wheel load while causing much less damage to the roads. The lower contact pressures also meant that pneumatic tires did not have constantly climb out of deformations in the road, like solid tires and thus had a much lower rolling resistance [3]. A pneumatic tire also has the ability to absorb small impacts from the road without raising the center of the wheel, which reduces shock input on the vehicle [5]. While pneumatic tires had been around for years in bicycles, the convergence of situations including low-cost rubber and well-maintained condition of public roads helped provide an impetus for the change to them as is used today.

The first pneumatic tire was created by Robert W. Thomson in 1845. This tire was designed for a horse-drawn carriage and featured a leather outer casing with an internal rubber coated canvas air chamber. While his product was successful in greatly reducing rolling resistance, it never was widely adopted. The second appearance of the pneumatic tire was in 1888 when John Boyd Dunlop created a pneumatic tire for his son's bicycle. He was reading to exploit his invention but Thomson's earlier patent was discovered. Shortly after Dunlop's reinvention, hundreds of tires companies sprung up and tire improvements evolved quickly. Charles Kingston Welsh invented the first wire-beaded tire in 1890. In that same year William Bartlett designed the first detachable pneumatic tire. This tire had a stiff, wire-reinforced portion at the bottom of each sidewall which engaged the flange of the rim, a basic design still in use today. In 1895 the Michelin brothers made the first automobile tire based on this detachable tire design. Starting in 1904, carbon black was added to the rubber to improve its strength and hardness. By 1940, the first fully synthetic rubber tires were being mass-produced [4].

Construction of Tires

Because of the number of different parties working on the development of the pneumatic tire, its evolution to its modern form did not follow a linear course, but progressed along multiple paths [2]. Despite this, rubber tires eventually dominated the market because of their properties are controllable in a manner allowing them to provide support and control with good durability in different conditions [6].

Modern tires can be split into two categories: radial and bias ply, yet both share many of the same basic features. First is the carcass, a molding of rubber reinforced by several layers of cords or fabric, each of which is called a ply. This carcass contacts the wheel at the bead and is inflated with air, which gives it tension. This tension is carried by non-rubber cords, the second major component of a modern tire. Cords are added because they have a higher modulus of elasticity than the rubber, while the rubber acts as a sealant to hold the gas pressure [6].

The original material used for reinforcement of the tire was square woven linen fabric. The linen was then replaced by cotton but this design proved unsuitable. As the tire deformed under load, the fabric distorted causing a sawing action in the cords which quickly damaged the cord material. This was solved by keeping the cords in place with a layer of rubber and removing the cross cords going perpendicular to the circumference of the tire. This produced a more even tension around the tire and allowed the cords to be bundled in a way that made them stronger than a woven fabric. The next textile used was rayon, then nylon, and finally polyester. Polyester cords remain in use on passenger cars today [4].

Where radial and bias ply tires begin to differ is the orientation of the plies. In radial tires the cords run perpendicular to the circumference of the tire. This provides a flexible sidewall and a soft ride. Directional stability is provided by stiff fabric or steel wire which runs at about a 20° angle to the circumference. These belts help keep the tire flat on the road when cornering despite lateral deflection in the tire [1].

Fig. **1.1**

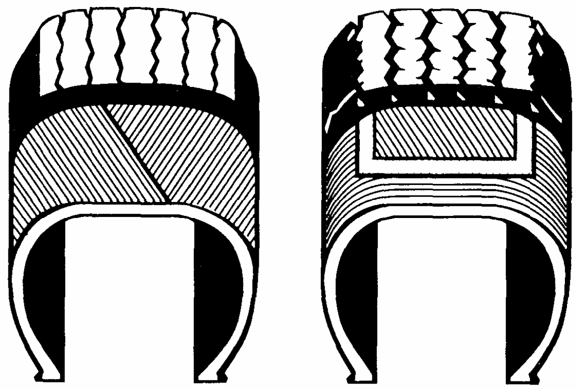

Fig. 1.1**: Comparison of Bias-ply and radial tires [1]**

Another important feature of the radial tire is the bead, the portion of the tire that contacts the lip of the wheel. To ensure that the tire is securely mounted, steel cords are usually built into the bead [2]. In bias ply tires the plies run at a 35-40° angle from the circumference and alternate in direction. Bias ply tires are laterally stiffer than radial tires but can squirm, e.g. the tread rolls under or moves, within the contact patch during cornering or tractive force generation. Bias ply tires were in use for passenger cars until the 1960's when radials were introduced [1]. Because of their many advantages, radial tires slowly took over and now radial tires are standard on nearly all production vehicles. These advantages include lighter weight, longer life, greater high-speed endurance, lower rolling resistance, superior load capacity, superior road adhesion, and les vehicle interior noise [5]. Bias ply tires are still in use on trucks and they have about half of the market share in this subcategory [1].

Another important component of all tires is the rubber used to make them and specifically the rubber in the tread. This rubber is worn down as it contacts the road and thus must have good wear characteristics. Selection of tire material is, however, a compromise between grip and durability. [6]

History of Vehicles

The first motorized vehicle appeared in 1796 and was built by Nicholas Joseph Cugnot, a French military engineer. He designed the three wheeled-steam driven vehicle in order to pull artillery pieces. It was almost another 100 years until the first practical automobiles, as we know them today, arrived on the scene. The credit for these first cars usually is given to Karl Benz and Gottlieb Daimler. Over the next ten years automobile design boomed. Some of the designers of these groundbreaking new vehicles include Armand Peugeot, Henry Ford, and Ransom Olds. Automotive breakthroughs continued on both sides of the ocean, but one of the most significant change occurred in 1908 when Henry Ford began mass-manufacturing the Model T in the US to market a vehicle that was truly affordable for most families. During this time, Daimler, Opel, Renault, Benz, and Peugeot were becoming renowned in Europe for vehicle design, and they quickly adopted the principles of Ford's modern production line. [1].

Automobiles advanced quickly and much of the early engineering focused on speed, comfort, and reliability. The speed of these new automobiles outpaced their development in other areas and turning and braking began to become more of an issue. Understanding of turning behavior was limited by the lack of comprehension of tire mechanics. This began to change in 1931, when a tire dynamometer, a device which could measure the mechanical properties of the pneumatic tire, was built. This machine allowed engineers to begin to independently study and isolate the turning behavior of automobiles independent of the chassis. This began the modern study of tire dynamics [1].

Tire Forces

In order to understand tire dynamics, the terminology and axis system are introduced. The most common vehicle coordinate system is the SAE vehicle axis system shown below in Fig. **1.2**. This system uses coordinates located at a vehicle's center of gravity.

Fig. **1.2**

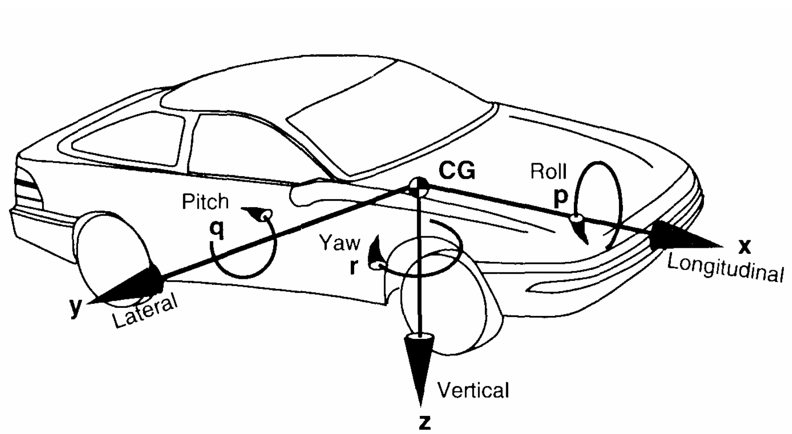

Fig. 1.2**: SAE Vehicle Axis System [1]**

Vehicle motion is usually described by the velocities (forward, lateral, vertical, roll, pitch, and yaw) relative to the body-fixed coordinate system. The body-fixed vehicle coordinate system must often be transformed to an earth-fixed coordinate system. The earth-fixed coordinate system is shown in Fig. **1.3** . In this system, the coordinates are: X for forward travel, Y for travel to the right, Z for vertical travel (positive in the downward direction), Ψ for the heading angle (the angle between x and X in the ground plane), v for the course angle (the angle between the velocity vector and the X axis), and β for the sideslip angle (the angle between the x axis and the vehicle velocity vector) [1].

Fig. **1.3**

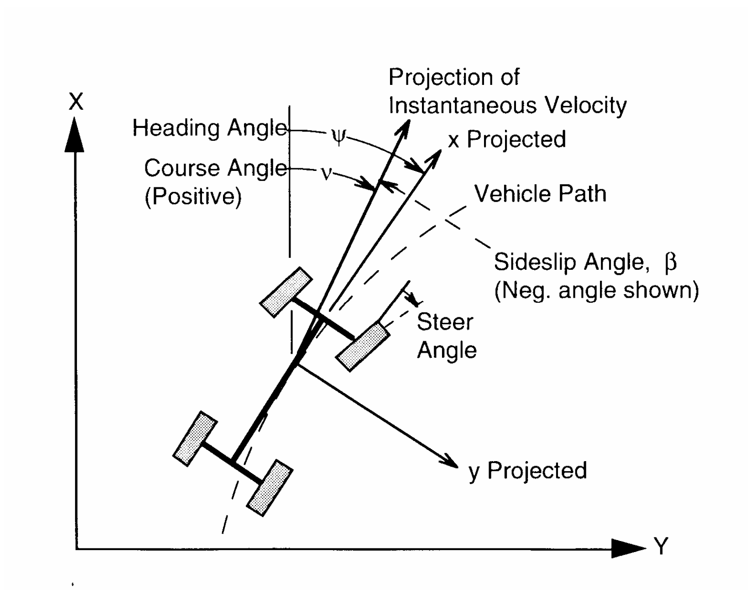

Fig. 1.3**: Vehicle in an Earth Fixed Coordinate System [1]**

The tires themselves also have their own coordinate system convention, as shown in Fig. **1.4**Error! Reference source not found.. The slip angle is the angle between the direction of wheel travel and the direction of the wheel heading. F_y, the lateral force, is also known as the cornering force, when the camber angle is zero. The camber angle is the angle of inclination of the wheel outward from the body of the car [1].

Fig. **1.4**

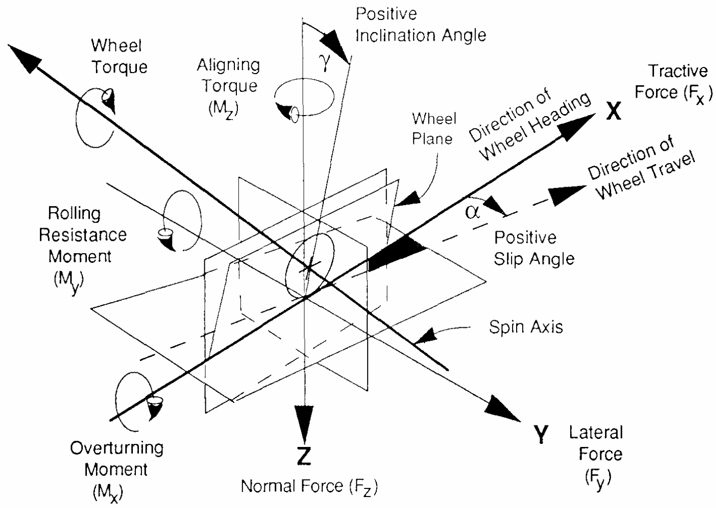

Fig. 1.4: **SAE tire axes and terminology[1]**

Different Tire Models

When analyzing the handling of a vehicle, it is necessary to represent the tire characteristics such that forces can be predicted from vehicle motion. One method is to use the construction data of a particular tire and/or finite element modeling. This is computationally expensive and difficult, but is commonly used in certain studies.

There are two other methods to achieve a tire representation more practical for general use: interpolation of a data table, or empirical equations. Data tables are easy to use but it is rare to have a table with a full comprehensive set of data. Empirical equations therefore dominate analytical tire models, and these can be split into two subcategories: those whose parameters represent physical properties or measures from a tire, and those whose coefficients don't have a direct tie to physical effects or properties of the tire. Equations of the former type use values such as vertical force, cornering stiffness and maximum cornering force. These equations are easier to comprehend because the parameters have physical meaning and are the focus of this thesis [1].

Linear Model

One of the most basic tire models is the linear model. This model assumes that the lateral force, F_y, increases with the slip angle at a given tire load. For low slip angles, this relationship is linear and described by equation Eq. **1.1** and shown in and described by equation Eq. **1.1** and shown in Fig. **1.5**

Fig. **1.5**

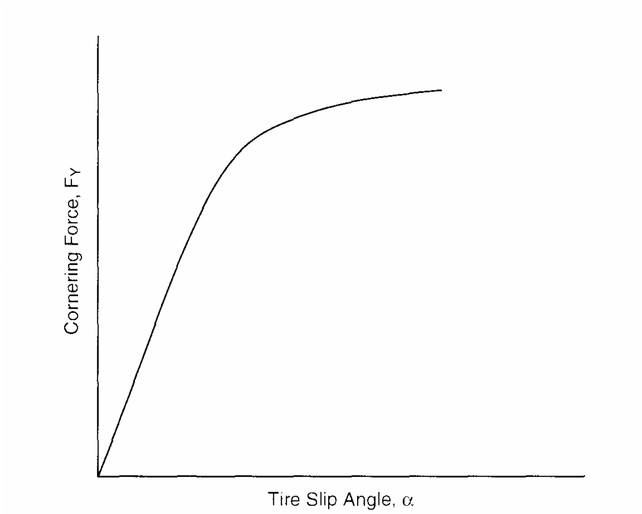

Fig. 1.5**: Change in lateral force, F_y, with changing slip angle, α for a constant vertical load and inflation pressure [5]. P. 57**

Eq. **1.1**

$$F_y = C_\alpha \alpha \tag{1.1}$$

Here C_α is the cornering stiffness. This constant is the negative of the slope of the graph of F_y versus α at the origin, according to SAE convention. This sign convention is imposed so that a positive slip angle produces a positive force on the tire. The cornering stiffness is dependent on many of the properties of the tire. Factors such as tire size, tire type, number of plies, cord angles, wheel width, and tread are all important variables for pneumatic tires. The most significant variables are the tire load and inflation pressure. The cornering forces are not significantly affected by the speed of the tire.

When using this model for steady state cornering analysis, it is convenient to represent the vehicle as a bicycle (Fig. **1.6**). This can be done because at high speeds the wheelbase of the vehicle is very small compared to the radius of a turn. The difference between steering angles of the inside and outside wheels can be assumed negligible and the two front wheels represented as one.

Fig. **1.6**

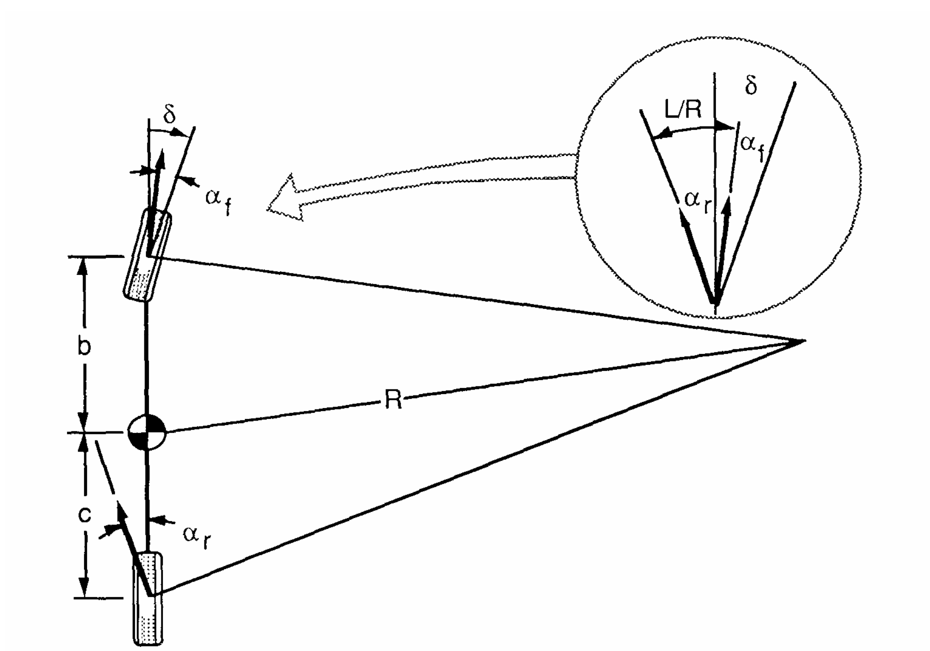

Fig. 1.6**: Linear Tire Model (Bicycle Model) [1]**

Brush Model

In the Brush Model, the tire is represented by a row of elastic bristles, called tread elements, which touch the road and can deflect in a parallel direction relative to the road. The brush model can be thought of as an analytical “bridge” between FEA and empirical methods. The compliance of the tread elements represents the combined elasticity of the elements of the tire. This is a relatively simple physical model that gives good qualitative results as compared with experiments. [7].

Fig. **1.7**

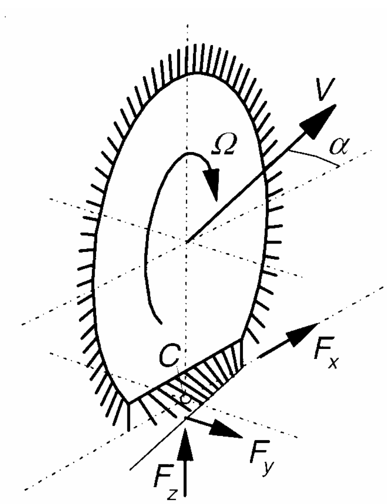

Fig. 1.7**: Brush Tire Model [7]**

Magic Tire Model

The best known and most widely used semi-empirical tire model is the so-called "Magic Tire" model. It is referred to as semi-empirical because the model is based on measured data but also contains structures that come from physical models [7]. This model was developed as a joint venture between Volvo Car Corporation and the Delft University of Technology. The goal was to develop a tire model which could accurately describe the characteristics of longitudinal force, lateral force, and self aligning torque in pure and combined slip situations [8]. According to Pacejka in the same reference, this tire model should:

- "be able to describe all steady-state tire characteristics,
- be easily obtainable from measured data,
- be physically meaningful; its parameters should characterize in some way the typifying quantities of the tire (This feature would make it possible to investigate the effect of changes of these quantities upon the handling and stability properties of the vehicle),
- be compact and easy to use,
- contribute to a better understanding of tire behavior,
- and be accurate" [8]

The general formula for this model is:

Eq. **1.2**

$$\mathbf{y = D \sin [C \arctan \{B\mathit{x}-E(B\mathit{x}-\arctan B\mathit{x})\}]} \quad 1.2$$

With

Eq. **1.3**

$$\mathbf{Y(X) = y(\mathit{x}) + S_V} \qquad 1.3$$

Eq. **1.4**

$$\boldsymbol{x} \mathbf{= X + S_H} \qquad 1.4$$

In these formulas Y(X) stands for side force, self aligning torque, or brake force. X stands for slip angle (α) or longitudinal slip (κ).

The coefficients are all meaningful and they represent the following:

B = stiffness factor

C = shape factor

D = peak value

E = curvature factor

S_H = horizontal shift

S_V = vertical shift [8]

The Magic Formula produces a curve as shown in Fig. **1.8** . The curve passes through the origin and reaches a maximum in the Y direction. The curve can be offset from the origin with the horizontal shift S_H and the vertical shift S_V [8].

Fig. **1.8**

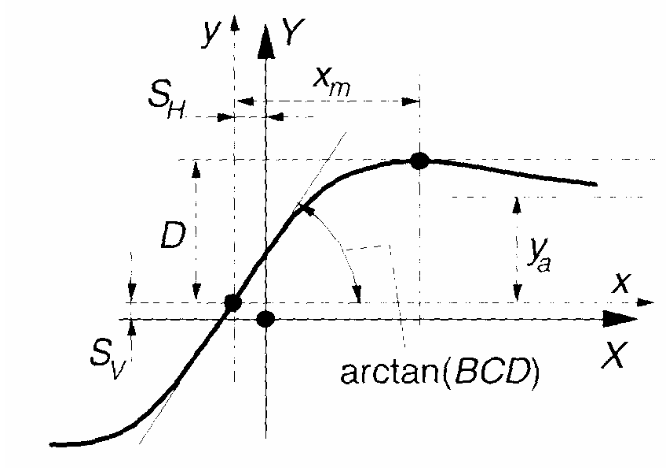

Fig. 1.8**: Curve Produced by the Magic Tire Model [7]**

1. Gillespie, T.D., *Fundamentals of Vehicle Dynamics*. 1992, Warrendale: Society of Automotive Engineers, Inc.
2. *Handbook of Automotive Engineering*, ed. H.-H. Braess and U. Seiffert. 2005, Warrendale: SAE International. 425.
3. Lay, M.G., *Ways of the World: A History of the World's Roads and of the Vehicles That Used Them*. 1992, New Brunswick: Rutgers University Press.
4. Committee, S.H., *The Automobile: A Century of Progress*. 1997, Warrendale: Society of Automotive Engineers, Inc. 48.
5. Donald Bastow, G. Howard, and J.P. Whitehead, *Car Suspension and Handling*. 4th ed. 2004, Warrendale: SAE International.
6. Dixon, J.C., *Tires, Suspension, and Handling*. Second ed. 1996, Warrendale, Pa: Society of Automotive Engineers, Inc. 621.
7. Pacejka, H.B., *Tire and Vehicle Dynamics*. 2nd ed. 2006, Warrendale: SAE International.
8. Bakker, E., H. Pacejka, and L. Lidner, *A New Tire Model with an Application in Vehicle Dynamics Studies*. 1989.

Chapter 2

Data Collection

This chapter details experimental testing of new tire designs for the macro to mega comparison of vehicle dynamics using the scale rolling roadway testbed, a new technology that was developed at Penn State University. Data from this simulator was used to calculate slip angles for the front and rear tires of the test vehicle. The different tire/wheel plate combination tested and the force calculations for the vehicle are also included in this chapter.

Background on Scale-Vehicle Data Collection

Because of the expense of full-size vehicle testing, academic research is often conducted using simulations. This is the same in the aerospace industry, where experimental aircraft are tested in scale form in wind-tunnels. Automotive simulations are much newer and were developed with the goal of allowing vehicles to be tested on a rolling roadway for safe, easy and economic studies of vehicle dynamics and control. Ideally for the tests to simulate highway conditions the vehicle should remain stationary and the simulated road surface move relative to the vehicle. This type of simulator is known as a Rolling Roadway Simulator (RRS) and a full size simulator like this is still very expensive to buy and maintain. For this reason, scale systems have been used for research in the past. These systems, however, were not Rolling Roadway Simulators and they operated simply by moving a scale vehicle along a fixed roadway. The first actual scaled Rolling Roadway Simulator was developed by a team including Sean Brennan at the University of Illinois, Urbana-Champaign. Other simulators of the same type are now in use at the United States Naval Academy and Auburn University but the Rolling Roadway Simulator at Penn State is unique for a number of reasons. This system allows the scaled vehicle, as well as the roadway itself, to move freely in both roll and pitch directions. Large roll angles of the treadmill can be used to create high lateral accelerations [1]. More information on this Rolling Roadway Simulator can been found in Appendix 2.

Fig. **2.1**

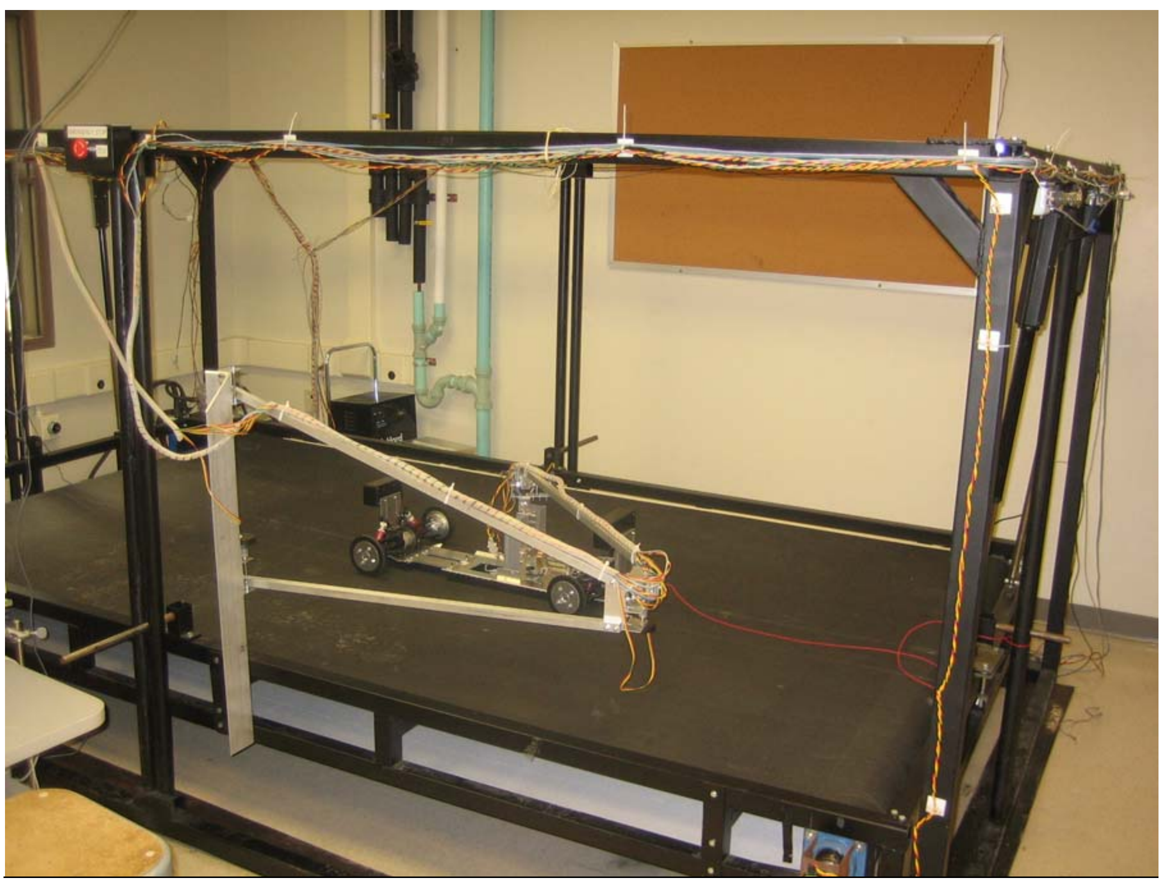

Fig. 2.1**: Rolling Roadway Simulator at Penn State University**

The roadway consists of a 12’ x 7’ treadmill powered by a brush DC motor which is controlled using a speed controller, giving the treadmill a top speed of 35 mph. The treadmill position is controlled by linear actuators in the roll and pitch direction, giving it a maximum roll angle of ±25° and a maximum pitch of ±6°. The vehicle is a 1/5th scale model car fitted with a four bar steering mechanism, double wishbone suspension at all four corners, and rack and pinion steering system powered by a brushless DC motor.[1].

The various control algorithms that allow the car to steer itself and maintain its position on the treadmill require that the vehicle’s position, orientation, and other states be known. This is accomplished through a sensing arm with five revolute joints which allow free movement in the roll and pitch directions while sensing the position and orientation of the vehicle through optical encoders at each joint. (Fig. **2.2**). Data from the optical encoders is combined with the fixed lengths of the arms to calculate the position and orientation automatically, allowing car to steer itself to maintain its position on the moving treadmill as the roll angle of the treadmill changes.

Fig. **2.2**

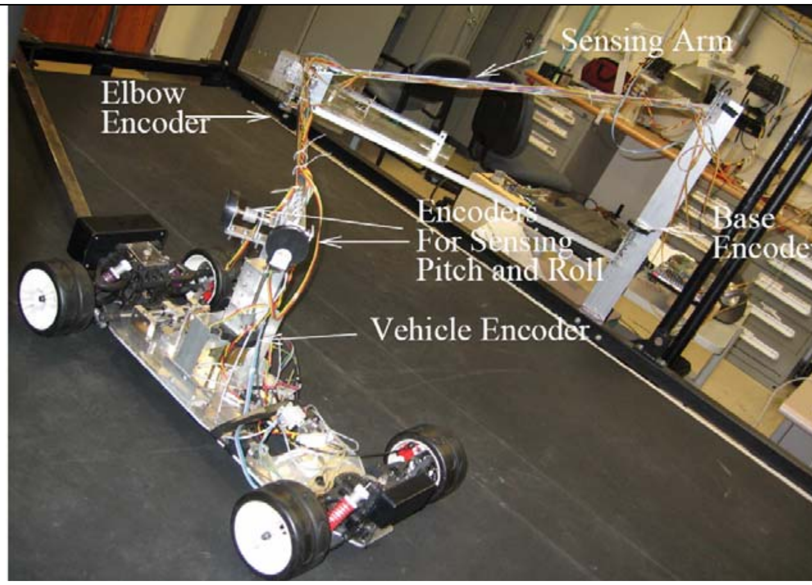

Fig. 2.2**: Sensing Arm [1]**

The car features solid rubber tires held which are bolted to the hubs and supported by aluminum disks on either side, as shown in Fig. Error! Reference source not found. Fig. Error! Reference source not found.

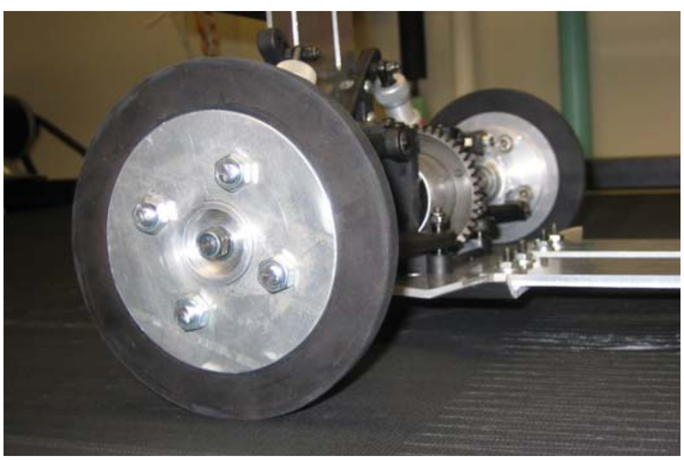

Fig. 2.3**: The solid rubber tires with aluminum plates on both sides.**

In order to test the ability to approximate the handling characteristics of real tires with these tires, a number of different configurations were tested. Larger wheel plates were drafted and cut from 6061 aluminum using a water jet cutter. The CAD drawing for these plates is shown in Fig. **2.4**.

Fig. **2.4**

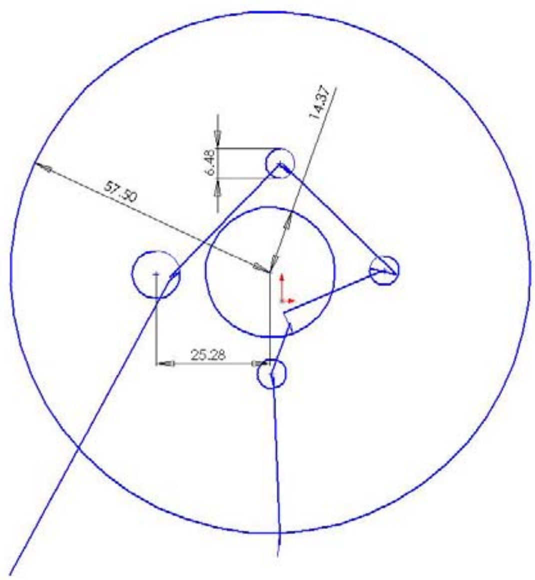

Fig. 2.4**: CAD rendering of new wheel plates with all dimension in millimeters**

These plates gave the tire a mere 2.9mm of sidewall length, as opposed to the original 15.925mm sidewall length. The difference between the original plates and the new plates is shown in Fig. **2.5**. A shorter sidewall length increases the sidewall stiffness of the tire..

Fig. **2.5**

Fig. 2.5**: Different Size Wheel Plates**

The car was also tested with two sets of tires (Fig. **2.7**) at each corner to effectively double the thickness of the tires. In order to accomplish this, a new set of tires, identical to the old ones, was constructed. The CAD drawing of these tires is shown in Fig. **2.6**. Longer bolts were used with the original hubs to accommodate the second set of tires.

Fig. **2.6**

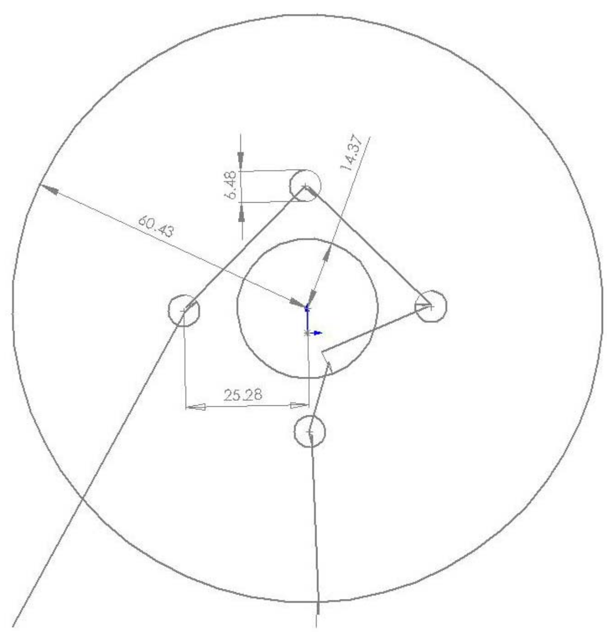

Fig. 2.6**: CAD rendering of tires with all dimension in millimeters**

Fig. **2.7**

Fig. 2.7**: Double tires versus single tires**

Physical measurements of the car were taken including the wheelbase (0.655m), the distance between the center of gravity and the front axle (.240m), and the distance between the center of gravity and the rear axle (.415m). The mass of the car is 11.4 kg. The physical data about the car was all measured by Sittikorn Lapapong. From these measurements and the data collected the slip angle and force in the Y direction were calculated. All these calculations were done using an Excel Spreadsheet which can be seen in Appendix 1.

For each test the roll angle of the treadmill was varied in increments of 2.5 degrees from 25 to -25 degrees and the steering motor output (radians) and yaw angle (degrees) of the car were recorded. The recorded data included the treadmill roll angle (in degrees), the steering motor angle (in radians), and the yaw angle of the car (in degrees). The steering motor angle data was centered for each test. This was done by subtracting the motor steering angle at a treadmill roll angle of zero from all the motor steering angles. Thus, when the treadmill was level in the roll direction, the steering angle was zero. The yaw angle data was also centered using this same method.

The motor steering angle which was recorded tells the angle of the pinion gear which is part of the rack and pinion steering system. From this angle the steering angle of the wheels can be calculated as follows: The rack and pinion gears have a diametral pitch of 120 and a pitch diameter of 0.5 in. By multiplying the diametral pitch and the pitch diameter the number of teeth on the pinion can be found to be 60. Then the number of radians per tooth can be calculated. This can then be converted to radians per inch movement of the steering rack by multiplying the radians per tooth by the diametral pitch (teeth per inch). The rack moves 12.564 rad/in which was converted to 494.65 rad/m. Using this data the steering angle of the motor in radians was converted to displacement of the steering rack in meters.

Fig. **2.8**

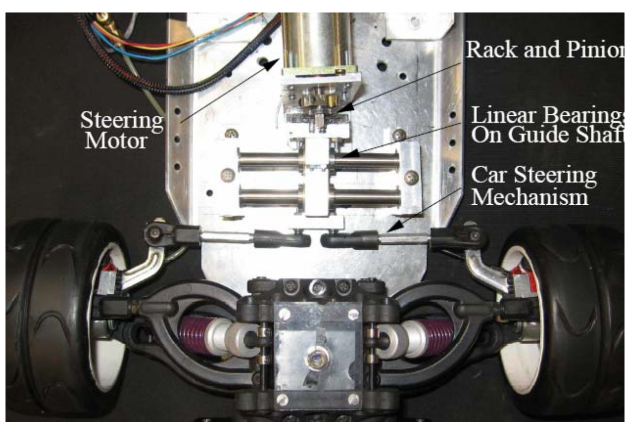

Fig. 2.8**: Close-up of rack and pinion [1]**

In Fig. **2.9** , *K* is the distance between the end of the steering arm and the center of the wheel hub and is constant. *S* is the length of the hypotenuse and is assumed to be constant for small steering inputs. The angle between *H* and *K* is assumed to remain 90° for small steering inputs. The length of *H* is variable according to the position of the steering arm. The length of *H* is its base length (its length when the steering is centered, 0.105m) plus or minus the length of change in the steering arm. This length of change of the steering arm was calculated from the steering motor angle as previously described. β can be calculated as the arcsine of *H* divided by *S*. For this suspension geometry β is 1.012467 radians when the steering is centered. Any change in β is the steering angle at the wheel.

Fig. **2.9**

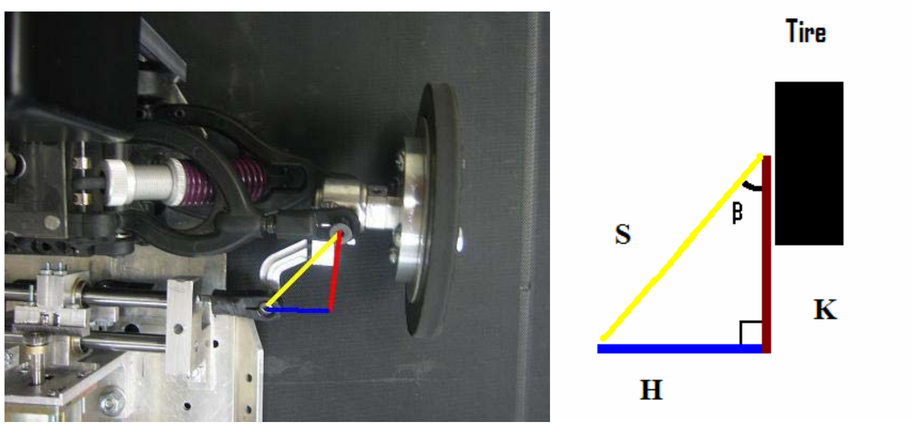

Fig. 2.9**: This suspension model was used to calculate the steering angle at the wheels from the motor steering angle**

Figure 3 shows a free body diagram of the car. The mass of the car is denoted by *m* (11.4 kg), the force of gravity by *g*, the distance from the center of gravity to the front axle by *a* (0.240m), the distance from the center of gravity to the rear axle by *b* (0.415m), and the wheelbase of the car by *L* (0.655m).

Fig. **2.10**

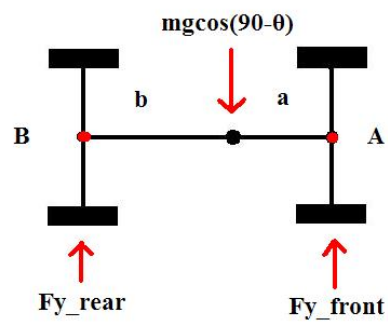

Fig. 2.10**: Free body diagram of the car on an incline with a roll angle of θ**

The force in the Y direction was calculated by summing the forces on the car and taking the moment about one of the axles. First the moment about point A was taken.

Eq. **2.1**

$$\sum M_A = mg\cos(90-\theta)(a) - (2)F_y\_rear(L) = 0 \qquad 2.1$$

In these equations F_y_rear and F_y_front refer to the lateral force on one tire. The forces are then summed in the Y-direction.

Eq. **2.2**

$$\sum F_Y = -mg\cos(90-\theta) + F_y\_rear\,\mathbf{(2)} + F_y\_front\,\mathbf{(2)} = \mathbf{0} \qquad 2.2$$

These equations can solved for the lateral forces on each tire:

Eq. **2.3**

$$F_{y\_}rear = \frac{mg\cos(90-\theta)(a)}{2L} \qquad 2.3$$

Eq. **2.4**

$$F_{y\_}\ front = \frac{mg\cos(90-\theta)-(Fy\_rear)}{2} \qquad 2.4$$

The front slip angle is the front wheel angle plus the yaw angle of the car. The front wheel angle was calculated previously and the yaw angle was read from the sensors. The rear slip angle is the yaw angle of the car.

Fig. **2.11**

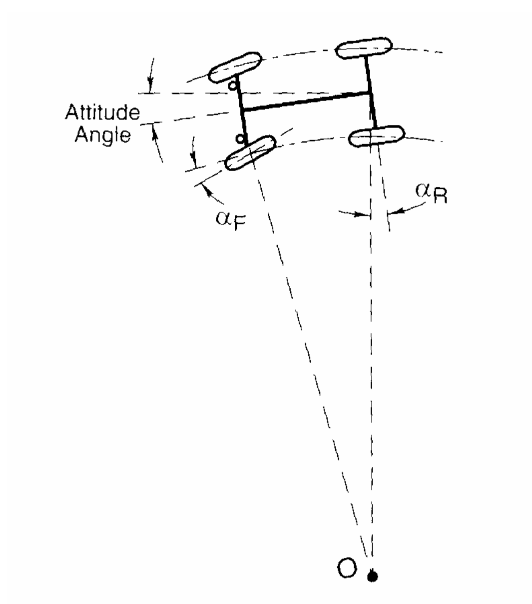

Fig. 2.11**: Front and Rear Slip Angle [2]**

The slip angle for both a front and a rear tire were plotted versus the slip angle. The slope of the linear portion of each of these graphs was the respective cornering stiffness for the front and the rear (Fig. **2.12**).

Fig. **2.12**

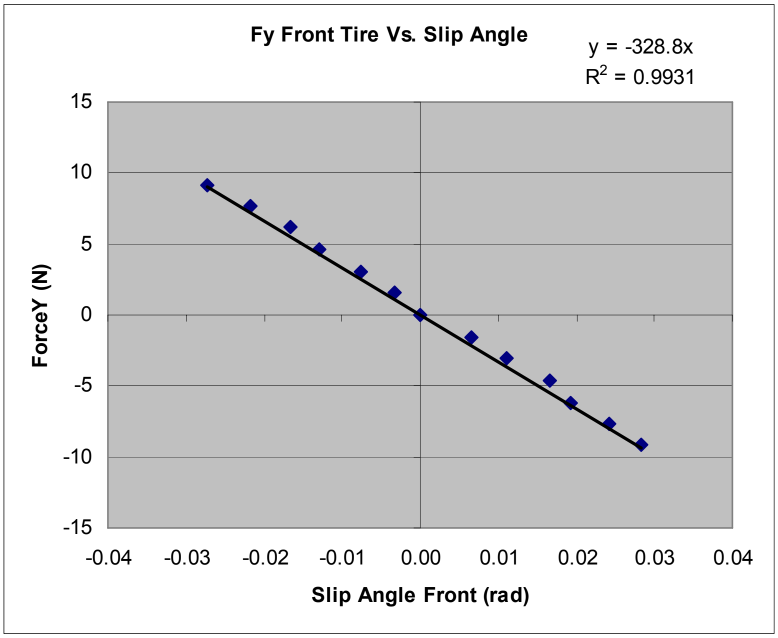

Fig. 2.12**: Graph used to find Cornering Stiffness**

1. Gupta, V., E. Callejas, and S. Brennan, *A Scaled Vehicle Test-Bed for Vehicle Dynamics and Control Studies*, The Pennsylvania State University.
2. Milliken, W.F. and D.L. Milliken, *Chassis Design: Principles and Analysis*, Warrendale: SAE International.

Chapter 3
Results, Data Analysis and Discussion

This chapter details experimental results as well as the analysis and discussion of those results. Data recorded from the rolling roadway simulator was used to calculate slip angle and cornering stiffness, which were then used to fit to the Magic Tire model to the experimental data using MATLAB. A least squares regression analysis was performed on the fitted data to ensure its validity.

The cornering stiffness values calculated from the raw data are shown below. The data for the first test was omitted because an error was found in the treadmill programming after the experiment, an error which led to incorrect values.

Fig. **3.1**

Test #	Tires	Plates	Treadmill Speed	Cαf N/rad)	Cαr (N/rad)
2	original	original	1	-328.8	-142.4
3	original	original	1	-333.46	-122.84
4	original	original	3	-352.26	-128.82
5	original	bigger	1	-442.95	-180.8
6	original	bigger	3	-490.97	-195.8
7	double	original	1	-378.81	-178.35
8	original	original	5	-378.19	-143.31

Fig. 3.1**: Cornering Stiffness Data Values**

The cornering stiffness Cα is equal to the product of the Magic Tire coefficients BCD, which were previously discussed in Chapter 1. A plot of the Magic Tire model is shown in Fig. **3.2** for reference.

Fig. **3.2**

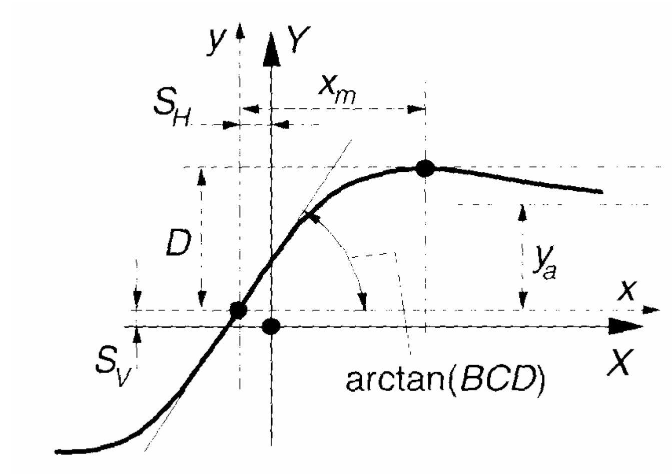

Fig. 3.2**: Curve Produced by the Magic Tire Model [2]**

The slope of a Magic Tire plot is equal to arctan(BCD) for the linear portion near the origin. For small values of BCD, arctan(BDC) = BCD is a good approximation. The D value is the peak force of the graph and C values are relatively stable around 1.3 [1]. This allows the B value to be calculated. The E value is chosen as -0.3 for a starting point, based on published values from other experimental data [1].

A Simulink diagram of the Magic Tire Model was constructed as shown in Fig. **2.12**. The BCDE values are input and F_y is generated for a range of slip angles. The effects of changing the coefficients BCDE can be seen in Fig. **3.4**. MATLAB was then used to graph the linear tire model, measured data, and the Magic Tire results together for both the front and rear for each test. The Magic Tire coefficients BCDE were adjusted from their initial starting points by hand to fit the curve of the actual data. One of these graphs is shown in Fig. **3.5**.

Fig. **2.12**

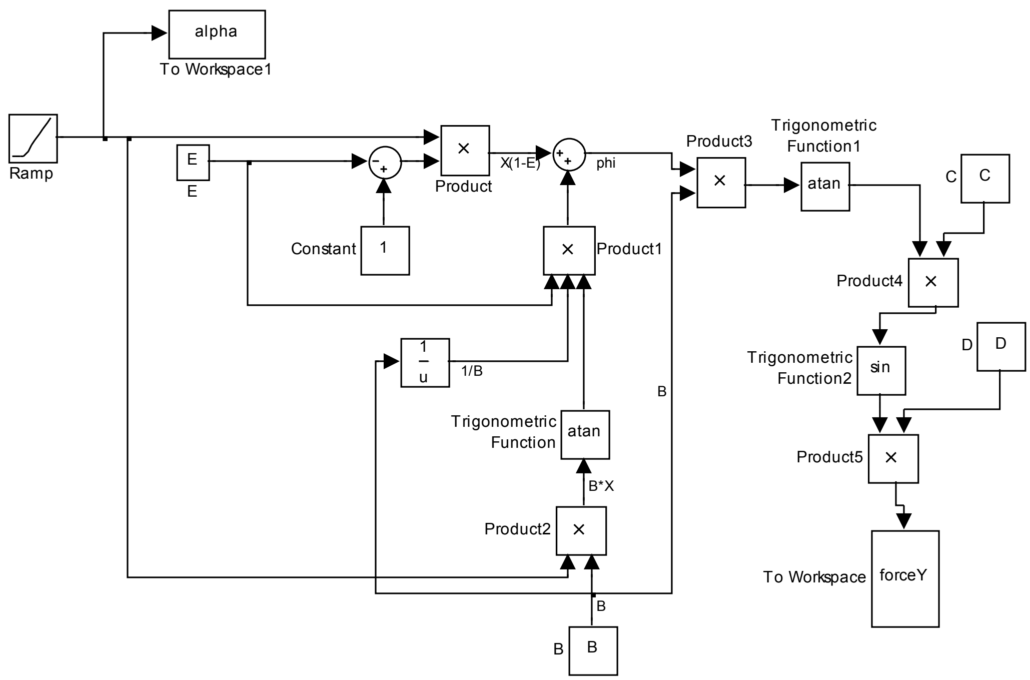

Fig. 3.3**: Simulink of Magic Tire Model**

Fig. **3.4**

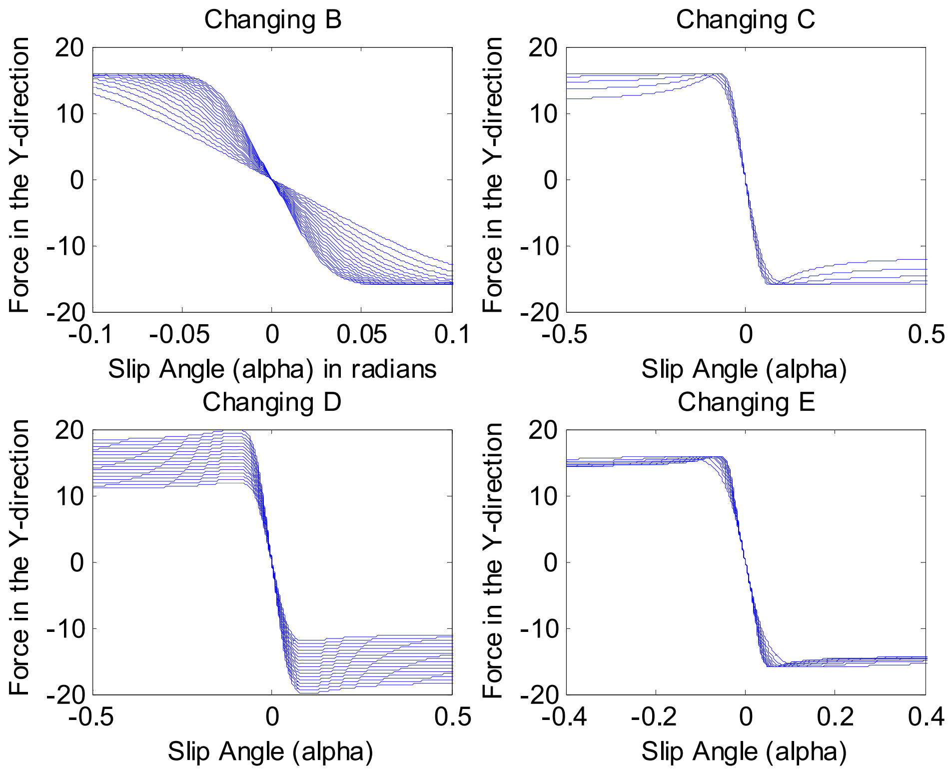

Fig. 3.4: **Effects of Changing Magic Tire Coefficients**

Fig. **3.5**

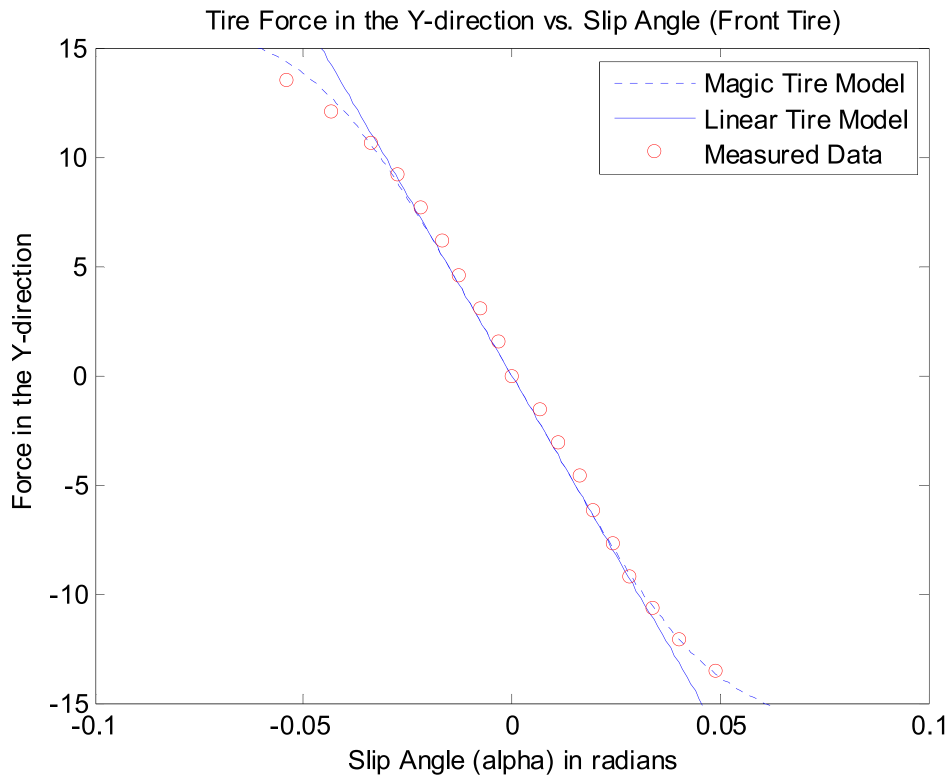

Fig. 3.5**: Hand-Fitted MATLAB Data**

Fitting the Magic Tire coefficients with accuracy and consistency proved difficult so MATLAB code was written to automatically fit the coefficients. This code uses the MATLAB function fminsearch, which finds the minimum of a scalar function when given starting estimates for the variables. Fminsearch relies on the simplex search method, a direct search method that doesn't use numerical or analytic gradients. The maximum limit for iterations was set to 4000. The error between the measured data curve and the calculated curve was also calculated. The data for a front wheel (Fig. **3.6**) and a rear wheel (Fig. **3.7**) and shown below.

Fig. **3.6**

Test #	B	C	D	E	error
2	-0.1709	317.0438	9.5015	16.2996	403.6024
3	-21.7461	0.2486	66.1588	0.453	0.802
4	-20.2231	1.1758	14.8608	-2.0295	6.5976
5	-8.8661	3.5597	14.8387	-1.0228	9.8771
6	-3.643	9.4493	14.8337	-0.0051	12.9908
7	-1.6287	17.6088	15.6894	-0.3841	45.1328
8	-32.1376	0.456	28.2258	-0.7478	8.2376

Fig. 3.6**: Autofitting BCDE for a Front Tire**

Fig. **3.7**

Test #	B	C	D	E	error
2	-1.8114	10.3887	8.1248	0.6837	1.0776
3	-13.5861	0.5514	16.9844	-0.7061	0.6015
4	-11.1943	1.2983	8.6402	-2.8522	0.897
5	-1.939	10.5986	9.3087	-1.6234	1.9377
6	-2.6123	8.1457	9.5157	2.4016	2.2199
7	-2.0676	8.989	10.1417	-0.0235	3.4582
8	-16.1938	0.4004	23.7177	-0.2459	0.7165

Fig. 3.7**: Autofitting BCDE for a Rear Tire**

These new BCDE coefficients were used to construct new plots containing the measured data, Magic Tire model, and linear model. The linear model uses the newly determined coefficients also, as opposed to the earlier hand-fitted values. One of these plots is shown side by side with a plot using hand fitted coefficients in Fig. **3.8**. Not all of the hand-fitted curves were quite as good as the one shown.

Fig. **3.8**

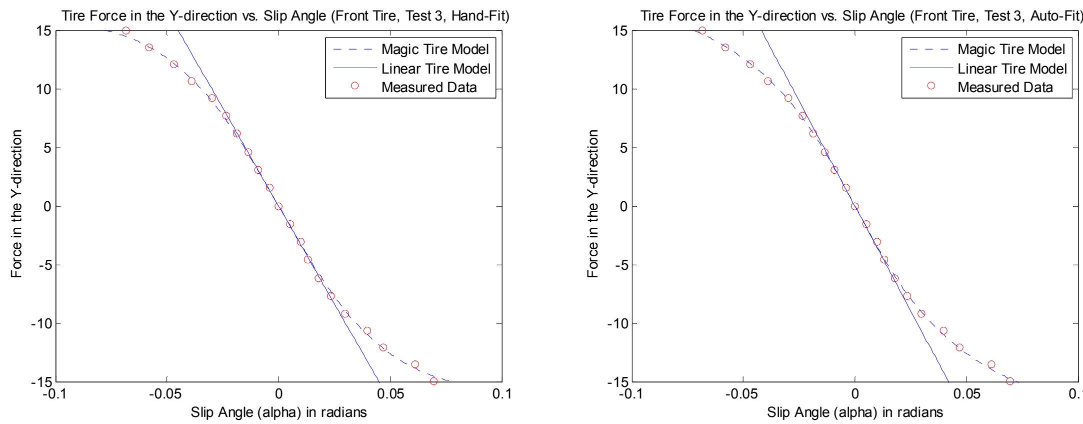

Fig. 3.8**: Hand-Fit data curve on the left versus Auto-Fit one on the right**

The plots produced from this auto-fit data are very good for the rear and overall good for the front. As can be seen from Fig. **3.6** and Fig. **3.7** , however, the BCDE values have a very wide spread. Some of the values found by this method were not within a reasonable range so this data was further examined by constraining one coefficient to see the effect it had on the others. Since C is known to be relatively fixed around 1.3 when using the Magic Tire model for cornering force, it was set as a constant [1]. This greatly improved the quality of the BDE values which are shown below in Fig. **3.9** and Fig. **3.10** with their respective values which were found earlier. The overall error between the experimental and modeled data remains about the same. The Magic Tire coefficients, however, are now in the same range from test to test.

Fig. **3.9**

Autofitting all values (front)					
Test #	**B**	**C**	**D**	**E**	**error**
2	-0.1709	317.0438	9.5015	16.2996	403.6024
3	-21.7461	0.2486	66.1588	0.453	0.802

4	-20.2231	1.1758	14.8608	-2.0295	6.5976
5	-8.8661	3.5597	14.8387	-1.0228	9.8771
6	-3.643	9.4493	14.8337	-0.0051	12.9908
7	-1.6287	17.6088	15.6894	-0.3841	45.1328
8	-32.1376	0.456	28.2258	-0.7478	8.2376
Autofitting BDE values (front)					
Test #	**B**	**C**	**D**	**E**	**error**
2	-18.4231	1.3	8.2018	-41.4577	539.5872
3	-14.5645	1.3	18.4583	0.7202	1.0378
4	-18.6453	1.3	14.8686	-1.5653	6.6737
5	-22.8202	1.3	15.5186	-1.5379	9.9596
6	-24.7119	1.3	15.0364	-2.461	12.6349
7	-20.1032	1.3	15.2944	4.1867	44.008
8	-20.2954	1.3	15.9938	-0.069	8.2648

Fig. 3.9**: Magic Tire coefficients for the front before and after fixing C value.**

Fig. **3.10**

Autofitting all values (rear)					
Test #	**B (1/rad)**	**C**	**D (N)**	**E (1/rad)**	**error**
2	-1.8114	10.3887	8.1248	0.6837	1.0776
3	-13.5861	0.5514	16.9844	-0.7061	0.6015
4	-11.1943	1.2983	8.6402	-2.8522	0.897
5	-1.939	10.5986	9.3087	-1.6234	1.9377
6	-2.6123	8.1457	9.5157	2.4016	2.2199
7	-2.0676	8.989	10.1417	-0.0235	3.4582
8	-16.1938	0.4004	23.7177	-0.2459	0.7165
Autofitting BDE values (rear)					
Test #	**B (1/rad)**	**C**	**D (N)**	**E (1/rad)**	**error**
2	-13.4539	1.3	8.4097	-1.9372	1.0649
3	-9.2497	1.3	10.6748	-0.4374	0.6068
4	-11.1822	1.3	8.6401	-2.8468	0.897
5	-14.7213	1.3	9.5429	-2.197	1.9051
6	-15.7149	1.3	9.5053	-2.0744	2.1685
7	-14.1533	1.3	9.6623	-2.8204	3.3461
8	-9.4352	1.3	12.5528	0.7105	0.7186

Fig. 3.10**: Magic Tire coefficients for the rear before and after fixing C value.**

As can be seen from Fig. **3.9** and Fig. **3.10** there is much less error in the fitted values for the rear. This is probably due to a number of factors. First is that the front slip angle is calculated using two recorded numbers, the yaw angle and the steering motor angle. The rear slip angle only uses the yaw angle in its calculation. Second is that the data for the rear is much more linear, making it easier to fit the curves. The rear tires experience less force in the vertical and lateral direction than the front because of the front weight bias of the car and thus for a given range of roll angles of the treadmill the rear tire curves are farther from their peaks. The data fit curves have been included in their entirety below (Fig. **3.12**- Fig. **3.25)**.

It should be noted that the Magic Tire coefficients found by this method still vary from published values found for real tires. The BDE values are dependent on the vertical force on the tire F_z so the published values were scaled down to the 1/5 scale car. This was done using the following equations from Wong [1]:

Eq. **3.1**

$$D = a_1 F_z^2 + a_2 F_z \qquad 3.1$$

Eq. **3.2**

$$BCD = a_3 \sin[a_4 \arctan(a_5 F_z) \qquad 3.2$$

Eq. **3.3**

$$B = \frac{BCD}{CD} \qquad 3.3$$

Eq. **3.4**

$$E = a_6 F_z^2 + a_7 F_z + a_8 \qquad 3.4$$

The C value is independent of F_z and is approximately 1.3. The F_z for the test car was calculated to be 35.43 N in the front and 20.49 N in the rear. The values scaled down from Wong are as follows : B_{front} = 17.80 1/rad, D_{front} = 35.79 N, E_{front} = 39.79 1/rad, Cαf = 828.37 N/rad, B_{rear} = 17.80 1/rad, D_{rear} = 20.71 N, E_{rear} = 40.09 1/rad, Cαr=479.08 N/rad [1]. The roadway simulator has previously been used by Garreth Murray to test the current scale car in a different configuration and with off-the-shelf scale tires. His results can be seen in Appendix 3. The F_z for the car at this time was 23.30 N. In this configuration the values were as follows for the one tire: B = 31.15 1/rad, C = 1.3, D = 13 N, E = -1.7 1/rad, and Cαf = 526.36 N/rad[3]. Fig. **3.11** shows values using Wong's Equations, Murray's values, and the author's values. The difference in sign for the B value and cornering stiffness is simply due to the use of different sign conventions.

Fig. **3.11**

	B (1/rad)	C	D (N)	E (1/rad)	Cαf (N/rad)
Author's Data	-18.65	1.30	14.87	-1.57	-360.40
Wong	17.80	1.30	35.79	39.79	828.37
Murray	31.15	1.30	13.00	-1.70	526.36

Fig. 3.11**: Type Caption Here**

These values cannot be compared directly as they based on different F_z values. It can be seen, however, that the scale of the values all match well except for Wong's E value, which is not comparable at all. Differences between the author's and Murray's values can be accounted for by the different tires used.

Fig. **3.12**

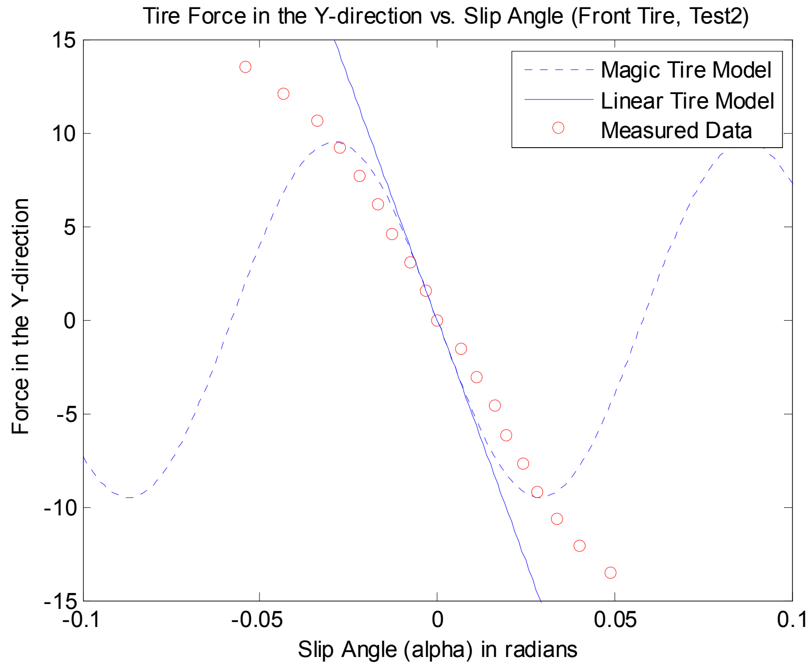

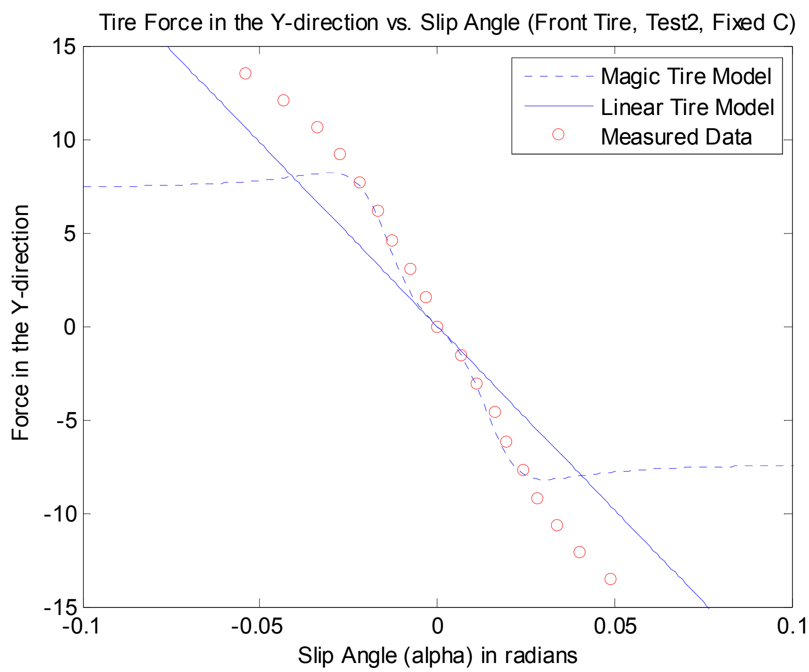

Fig. 3.12**: Plots for Test 2 for the front tire with all the values fitted and for the front tire with C fixed.**

It should be noted that the fit of the above data curves is an abnormality. In the first curve the unconstrained C value led to very unrealistic Magic Tire coefficients. The second curve, with a fixed C, is better but still not good. The linear curve and the Magic Tire model only have the same slope at the origin.

Fig. **3.13**

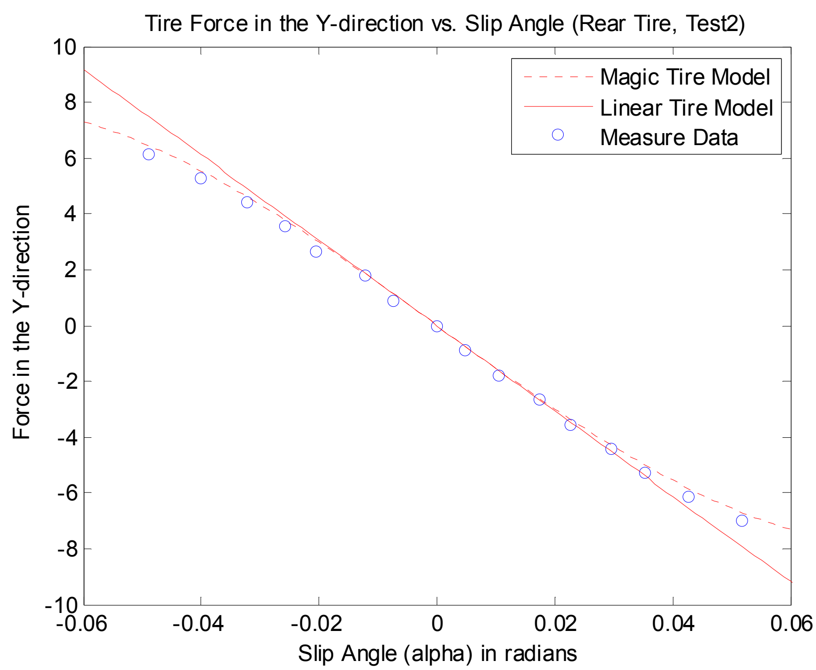

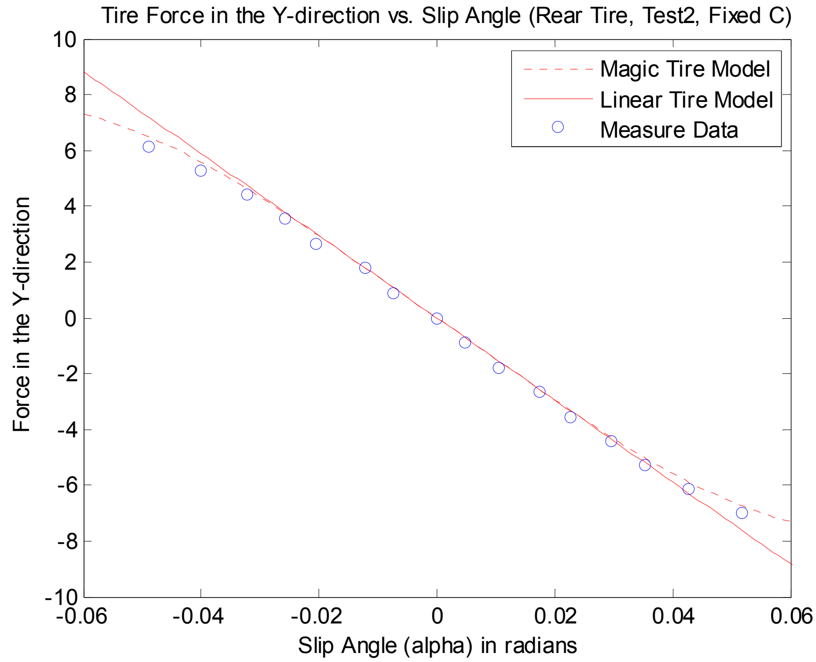

Fig. 3.13**: Plots for Test 2 for the rear tire with all the values fitted and for the rear tire with C fixed.**

Another possible source of error in the nonlinear fits, illustrated well in Fig. **3.13**, is that the nonlinearities are not excited very much. Only a few data points break away from the linear portion of the graph. This could be solved by recording data for a larger range of treadmill roll angles.

Fig. **3.14**

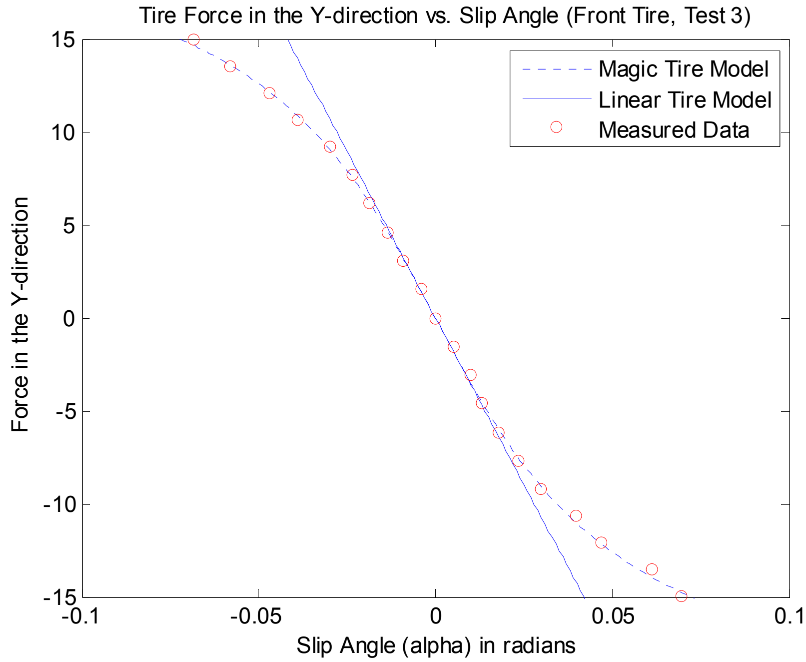

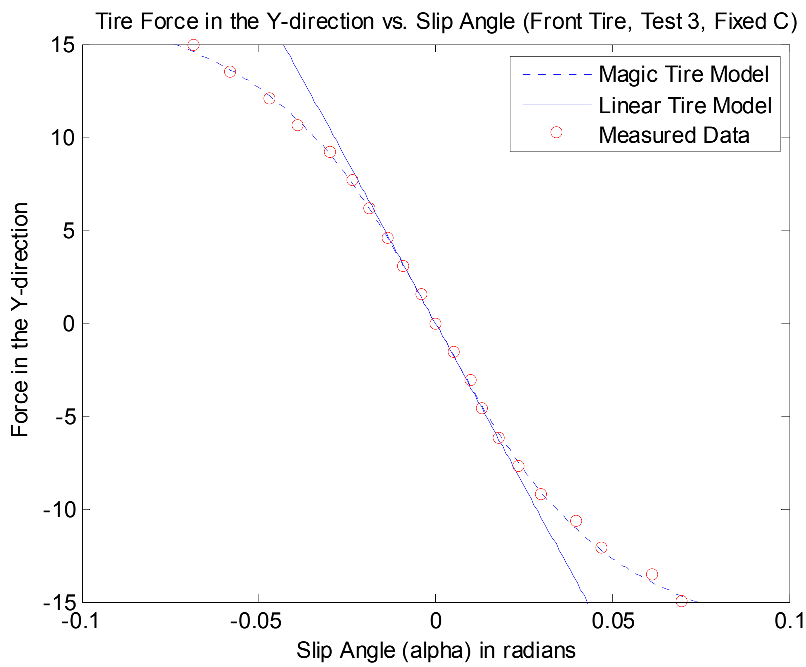

Fig. 3.14: **Plots for Test 3 for the front tire with all the values fitted and for the front tire with C fixed.**

Fig. **3.15**

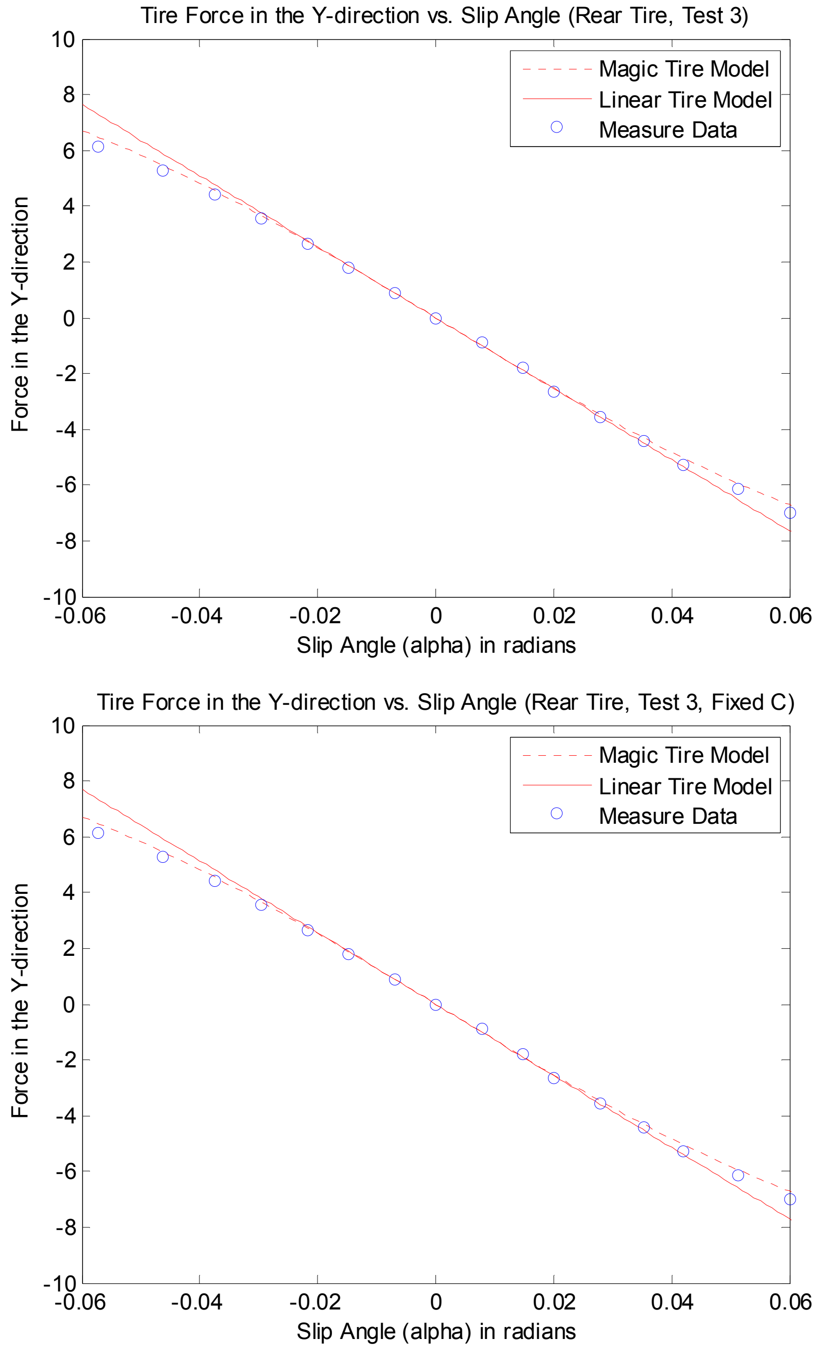

Fig. 3.15**: Plots for Test 3 for the rear tire with all the values fitted and for the rear tire with C fixed.**

Fig. **3.16**

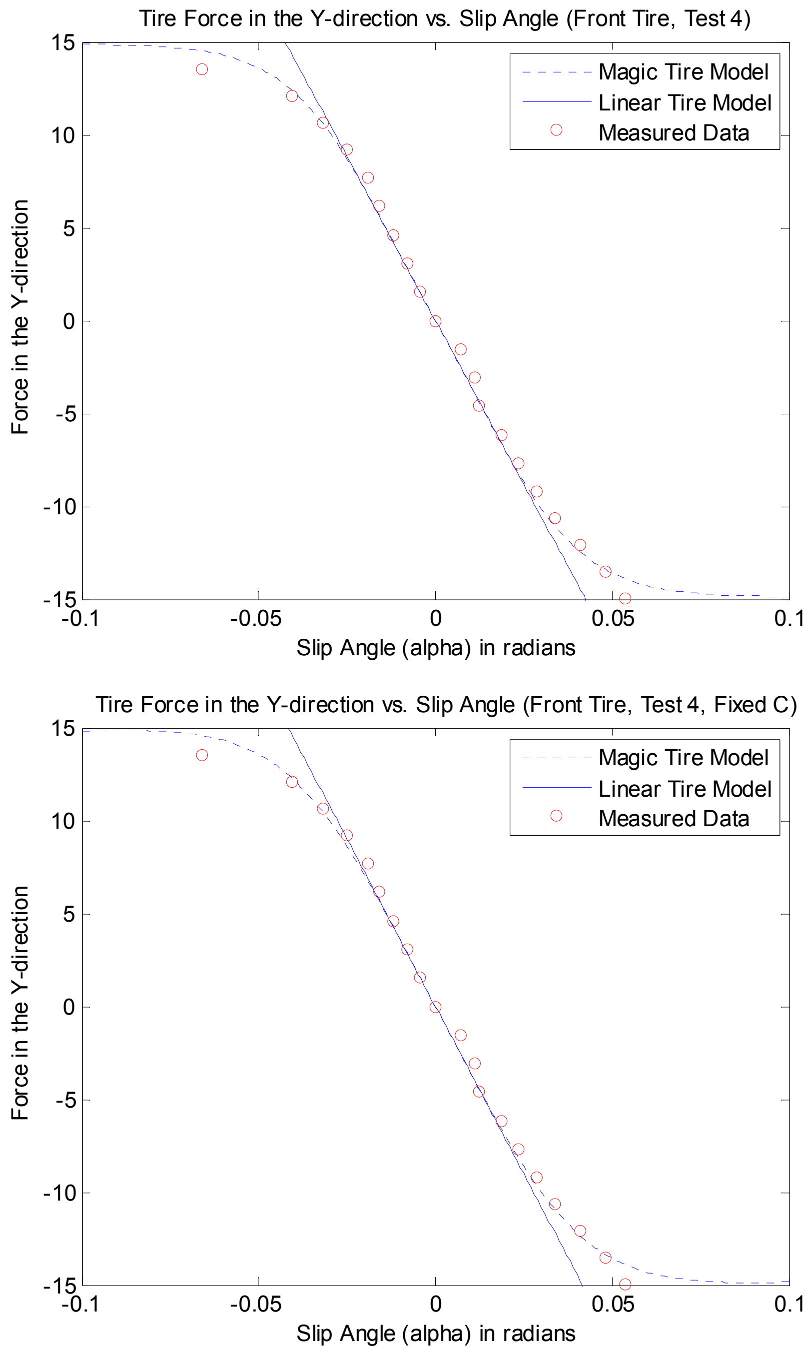

Fig. 3.16**: Plots for Test 4 for the front tire with all the values fitted and for the front tire with C fixed.**

Fig. **3.17**

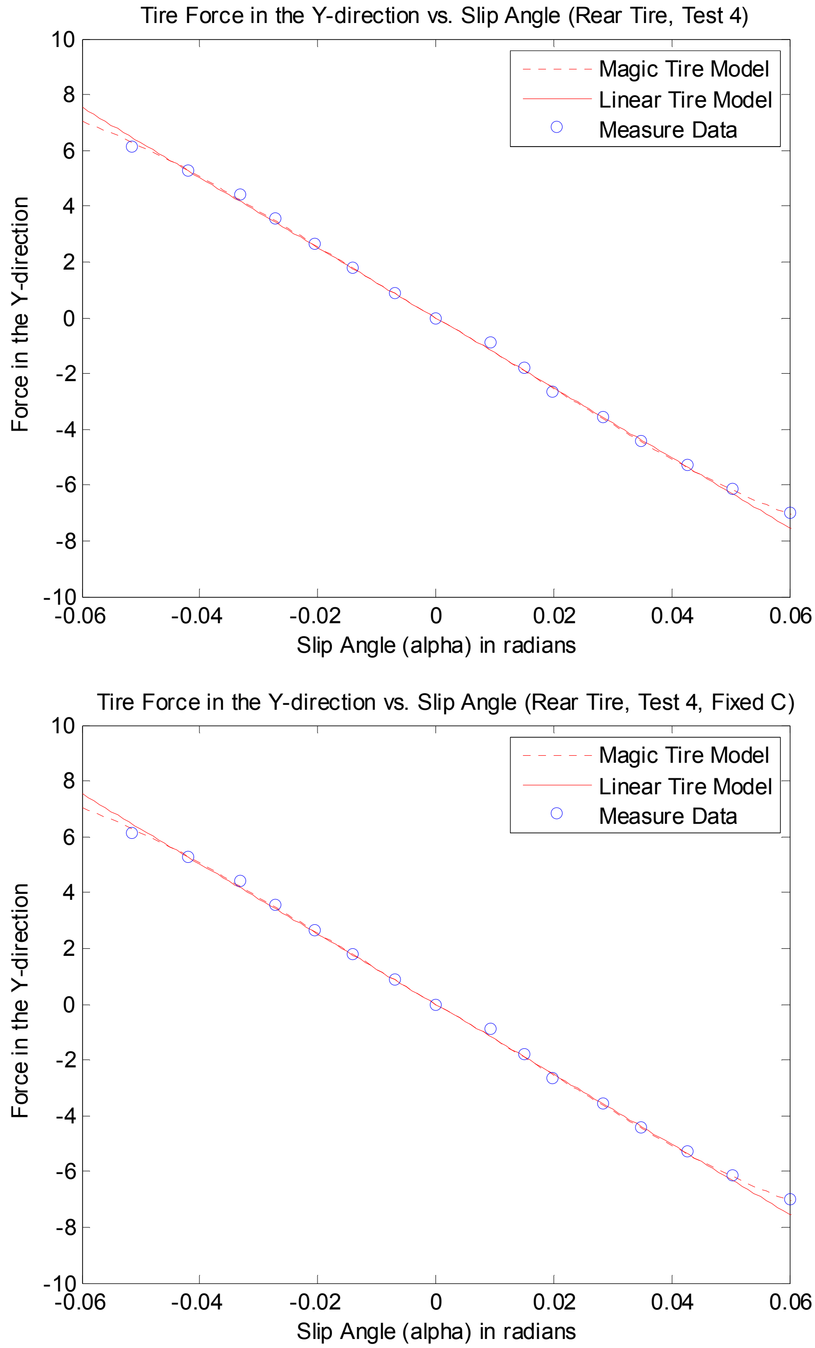

Fig. 3.17**: Plots for Test 4 for the rear tire with all the values fitted and for the rear tire with C fixed.**

Fig. **3.18**

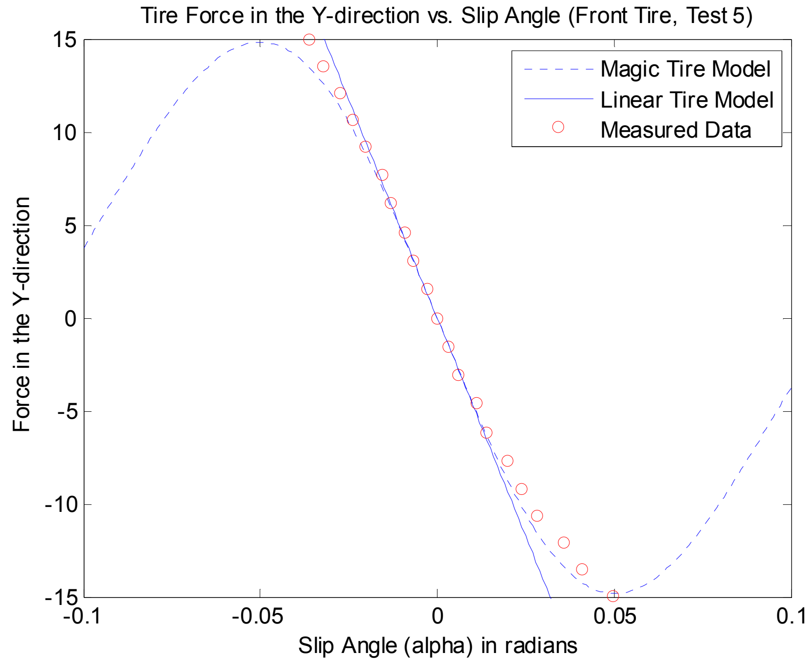

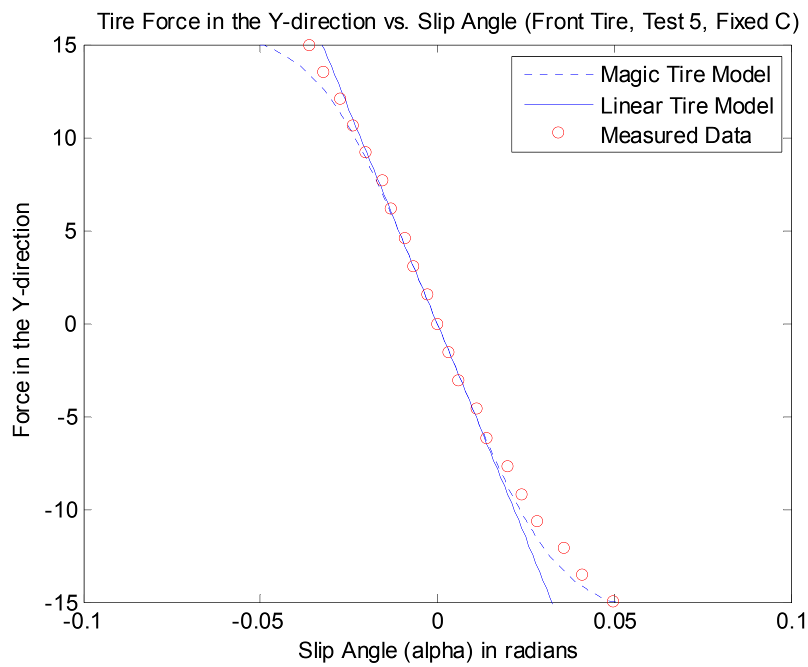

Fig. 3.18**: Plots for Test 5 for the front tire with all the values fitted and for the front tire with C fixed.**

Fig. **3.19**

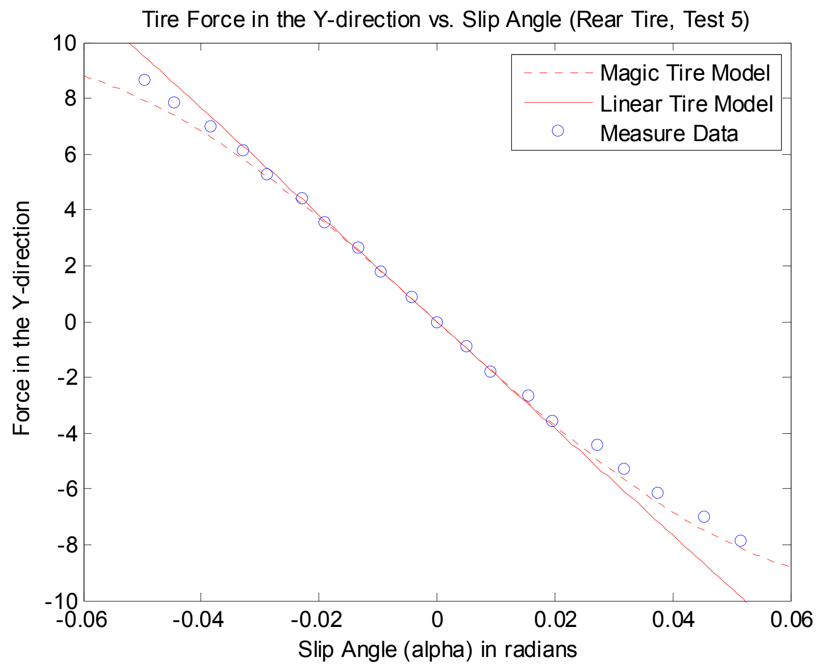

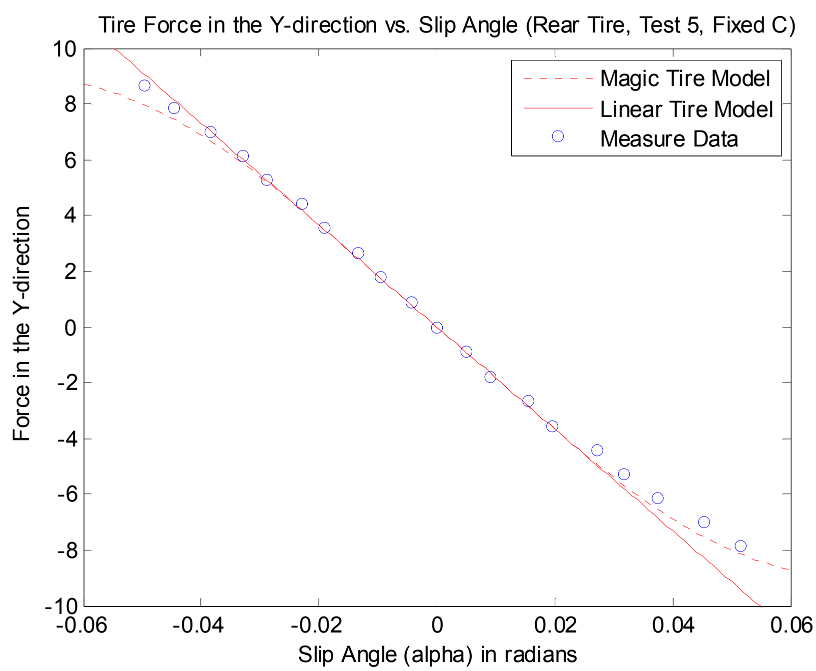

Fig. 3.19**: Plots for Test 5 for the rear tire with all the values fitted and for the rear tire with C fixed.**

Fig. **3.20**

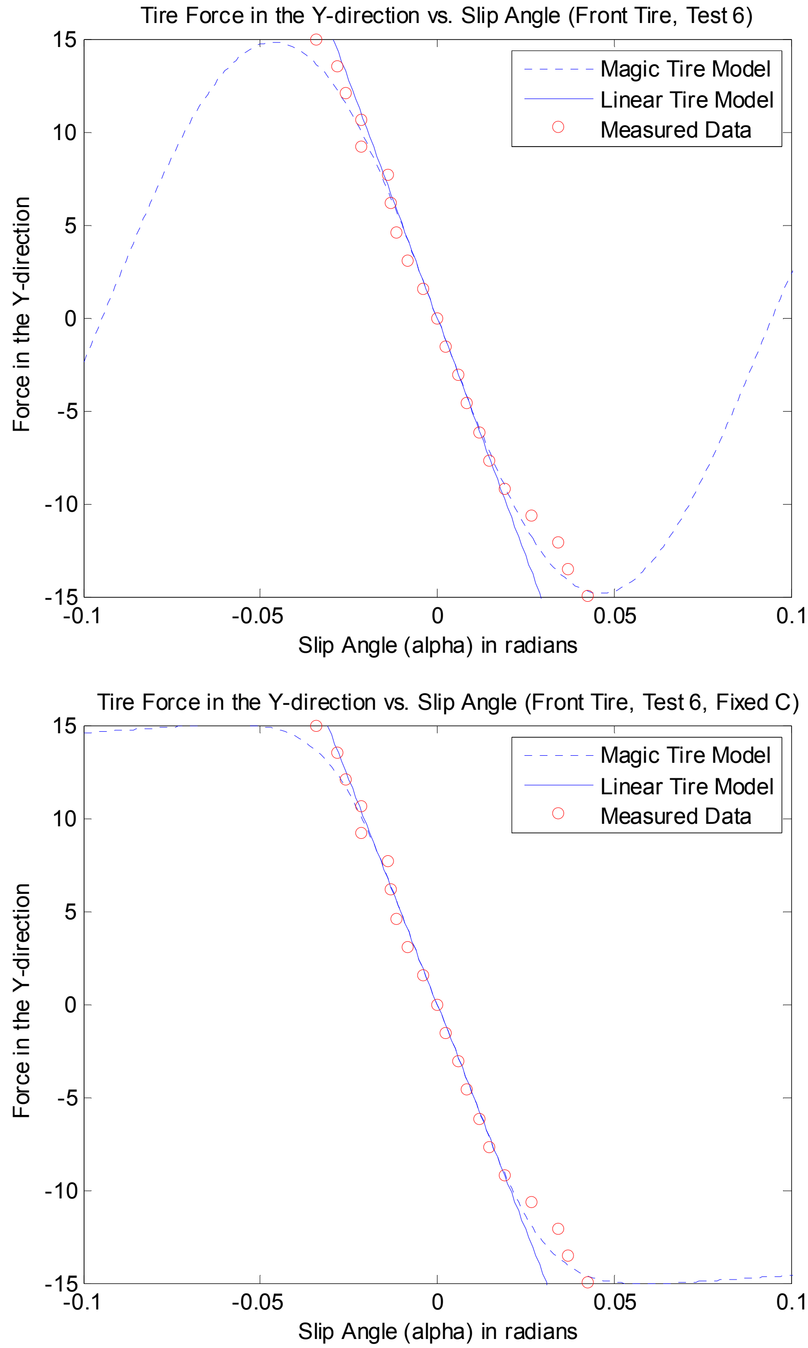

Fig. 3.20**: Plots for Test 6 for the front tire with all the values fitted and for the front tire with C fixed.**

Fig. **3.21**

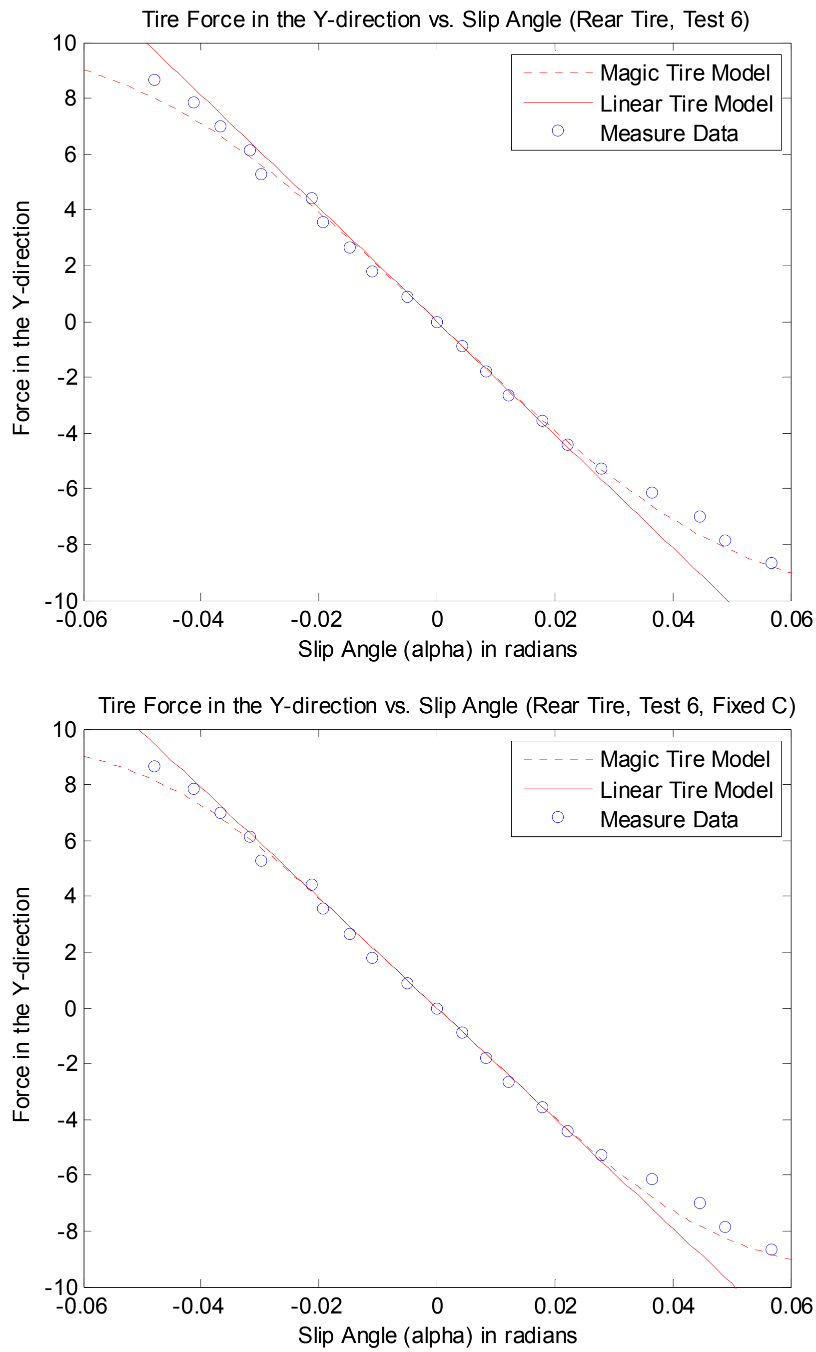

Fig. 3.21**: Plots for Test 6 for the rear tire with all the values fitted and for the rear tire with C fixed.**

Fig. **3.22**

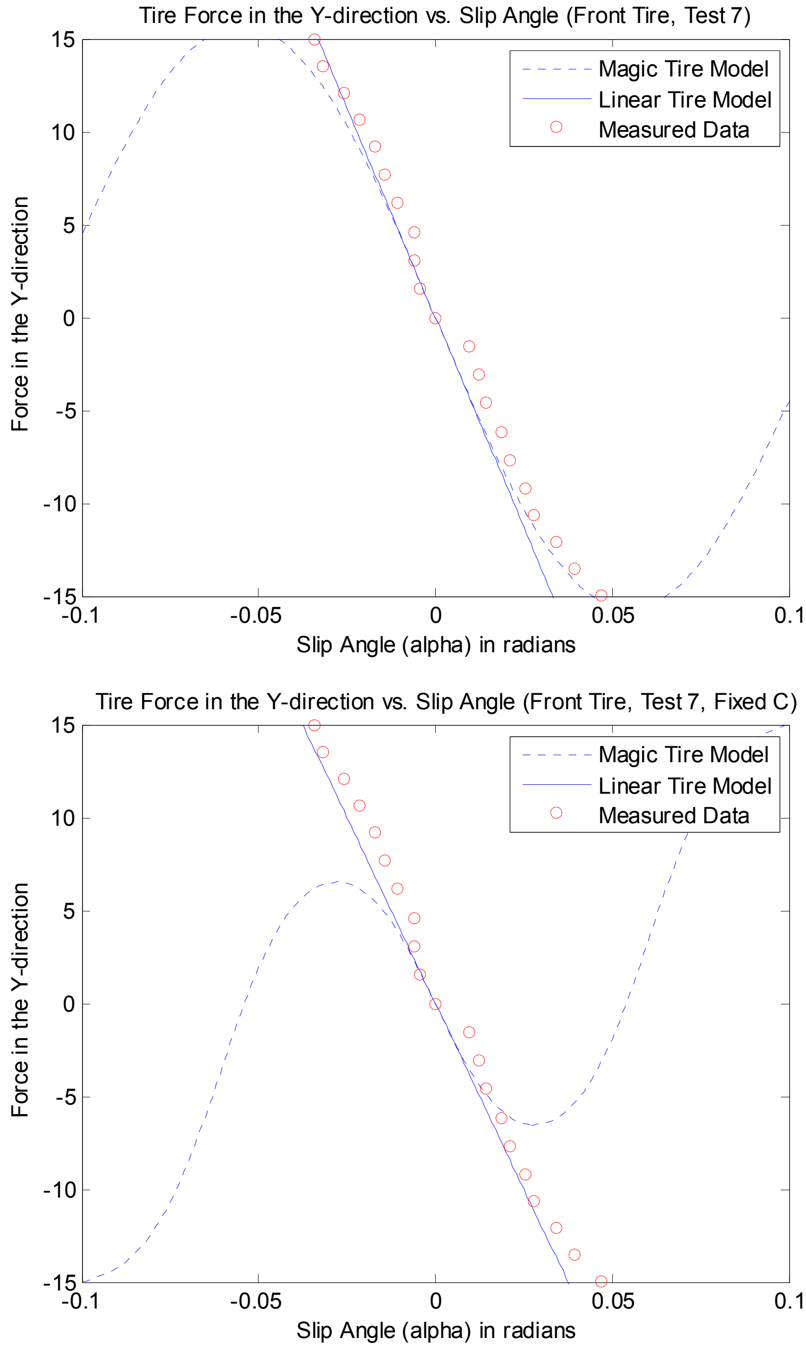

Fig. 3.22**: Plots for Test 7 for the front tire with all the values fitted and for the front tire with C fixed.**

Fig. **3.23**

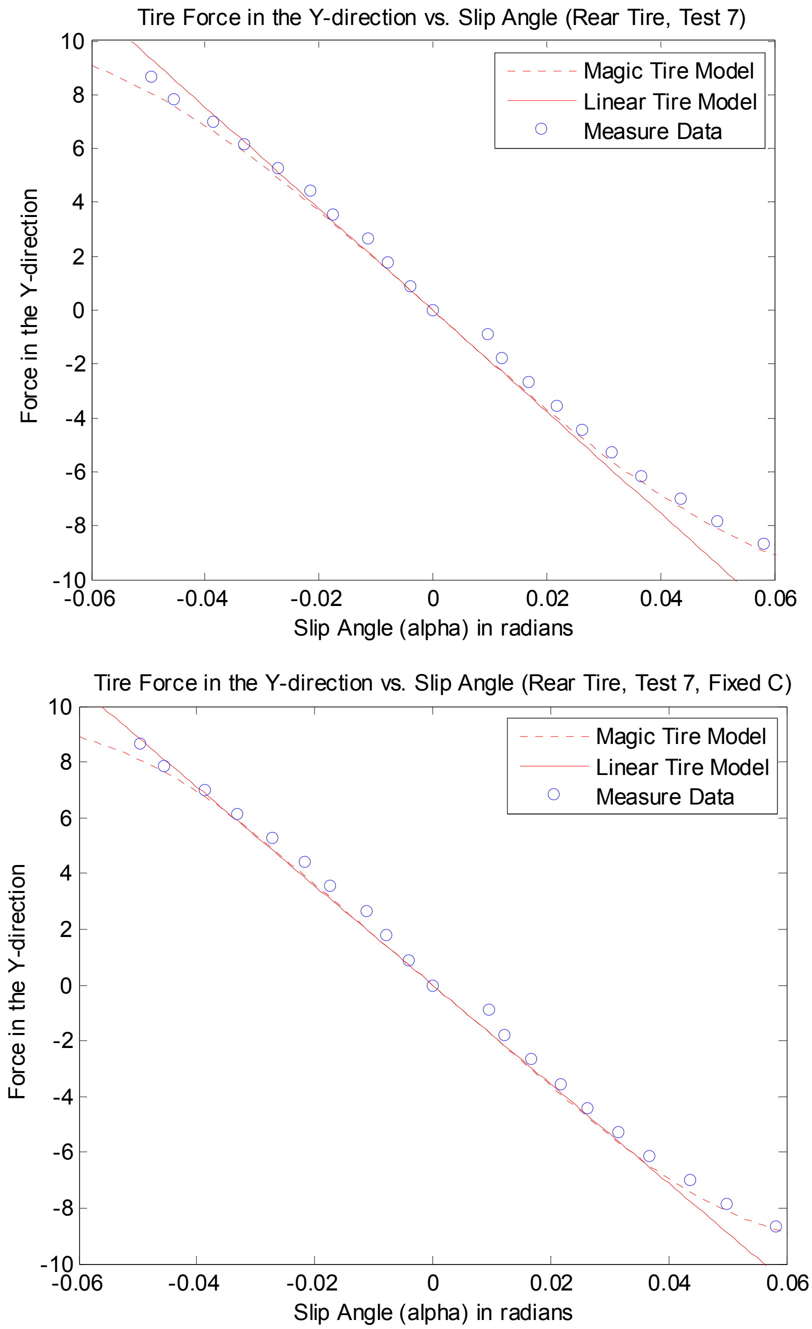

Fig. 3.23**: Plots for Test 7 for the rear tire with all the values fitted and for the rear tire with C fixed.**

Fig. **3.24**

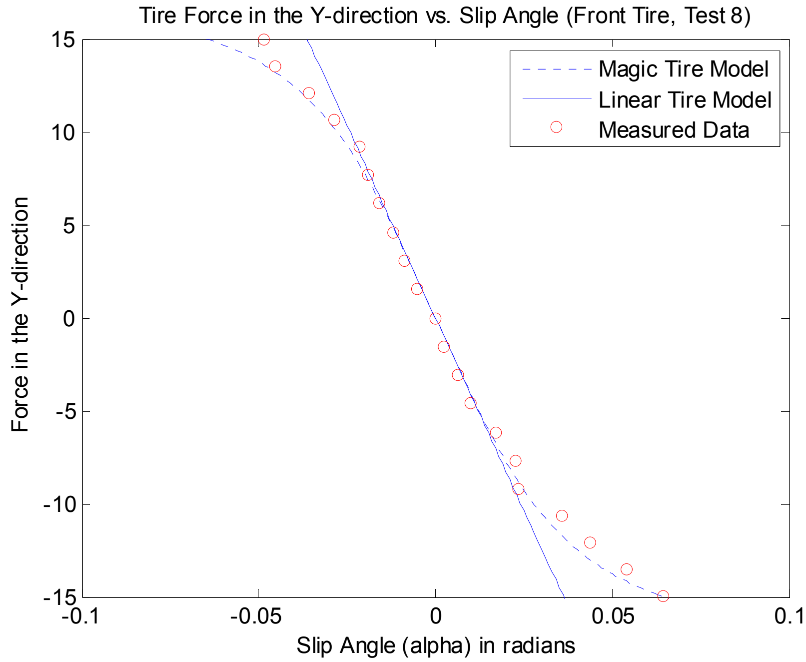

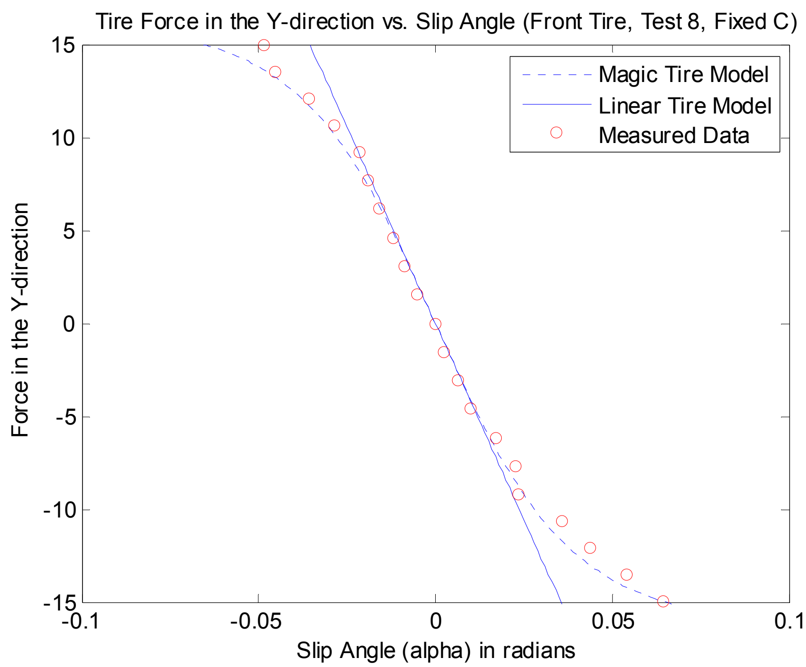

Fig. 3.24: **Plots for Test 8 for the front tire with all the values fitted and for the front tire with C fixed.**

Fig. **3.25**

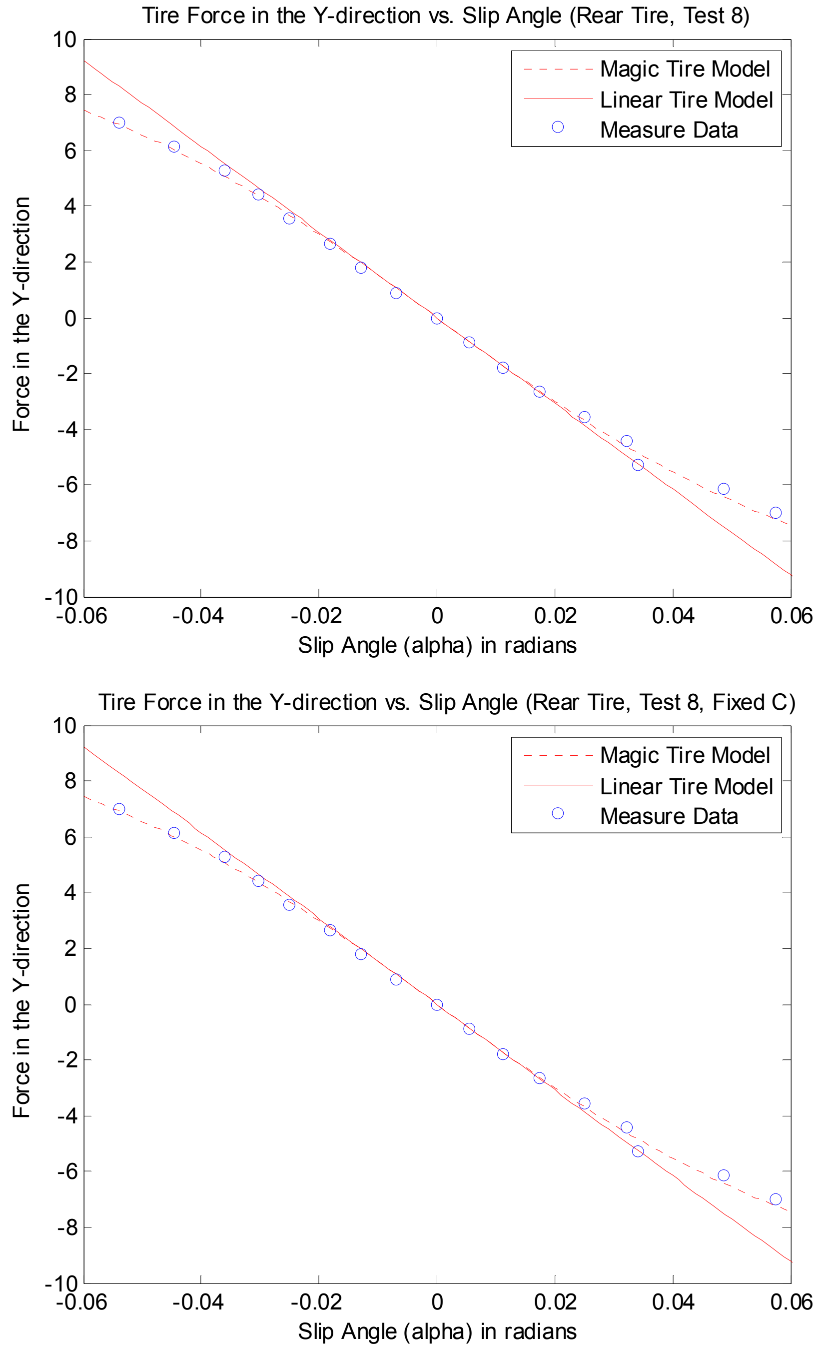

Fig. 3.25: **Plots for Test 8 for the rear tire with all the values fitted and for the rear tire with C fixed.**

Now that the BCDE values are reasonable and have been standardized, the next step is to analyze what effect the three test variables (number of tire laminates, sidewall thickness, and treadmill speed) had on the cornering stiffness and the BCDE values. If the changes in BCDE values can be attributed to a specific variable, then in the future these variables can be used to construct tires with specified properties. This was done by performing a least-squares linear regression analysis. The basic format of the regression analysis is the matrix shown in Eq. **3.5**.

Eq. **3.5**

$$\begin{aligned} y_1 &= a_1 x_{11} + a_2 x_{21} + a_3 x_{31} \\ y_2 &= a_1 x_{12} + a_2 x_{22} + a_3 x_{32} \\ y_n &= a_1 x_{1n} + a_2 x_{2n} + a_3 x_{3n} \end{aligned} \tag{3.5}$$

The *y* values are the variable being investigated (for example Cαf). The *x* values are as follows: x_1 is the number of tire laminates, x_2 is the sidewall length, and x_3 is the treadmill speed. The *a* values are what is solved for and they tell what effect each *x* value has on each *y* value. X and Y matrixes are constructed and A is solved for using Eq. **3.6**. Y-bar values are found using Eq. **3.7.**

Eq. **3.6**

$$A = (X^T X)^{-1} \cdot (X^T Y) \tag{3.6}$$

Eq. **3.7**

$$Y = X \cdot A \tag{3.7}$$

The regression analysis for the front and rear cornering stiffness are shown below. Regression analysis was performed for BDE values for both the front and the rear. The data from test 8 was an outlier and was removed from all of the regression analyses. This is possibly due to a problem with the steering linkage, which came apart shortly after that test was completed.

Fig. **3.26**

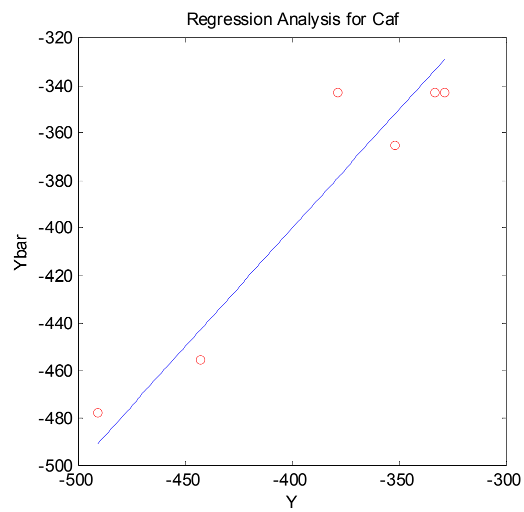

Fig. 3.26**: Regression analysis for front cornering stiffness.**

Fig. **3.27**

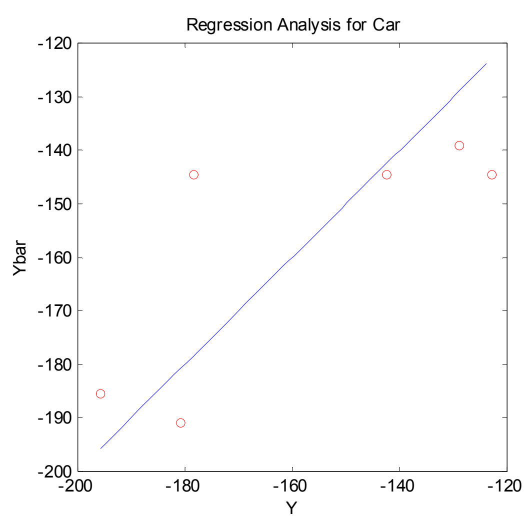

Fig. 3.27**: Regression analysis for rear cornering stiffness**

Fig. **3.28**

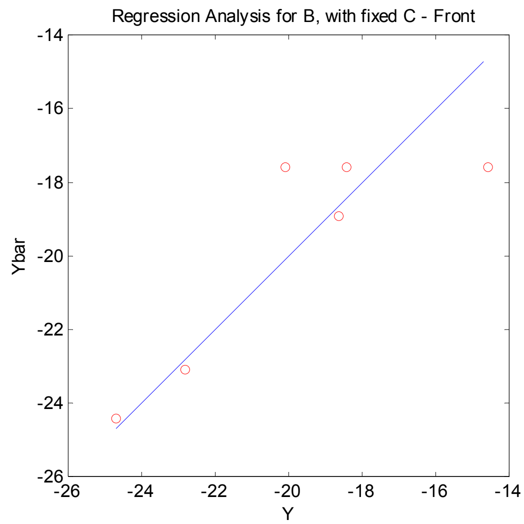

Fig. 3.28**: Regression analysis of B values for the front wheel, with C fixed**

Fig. **3.29**

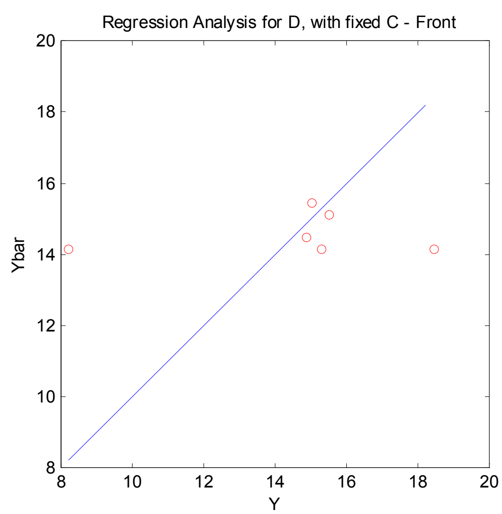

Fig. 3.29**: Regression analysis of D values for the front wheel, with C fixed**

Fig. **3.30**

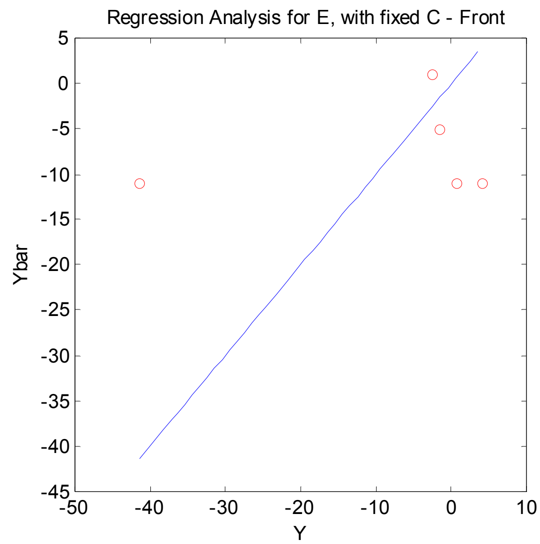

Fig. 3.30**: Regression analysis of E values for the front wheel, with C fixed**

Fig. **3.31**

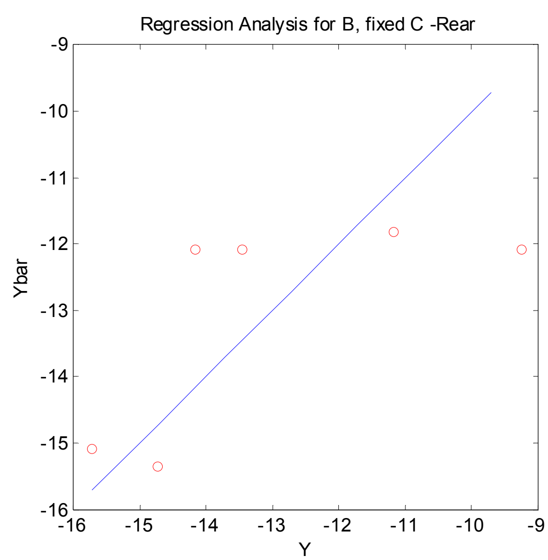

Fig. 3.31**: Regression analysis of B values for the rear wheel, with C fixed**

Fig. **3.32**

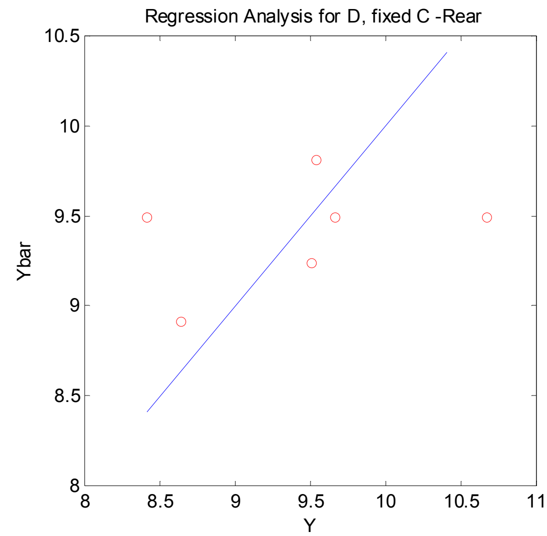

Fig. 3.32**: Regression analysis of D values for the rear wheel, with C fixed**

Fig. **3.33**

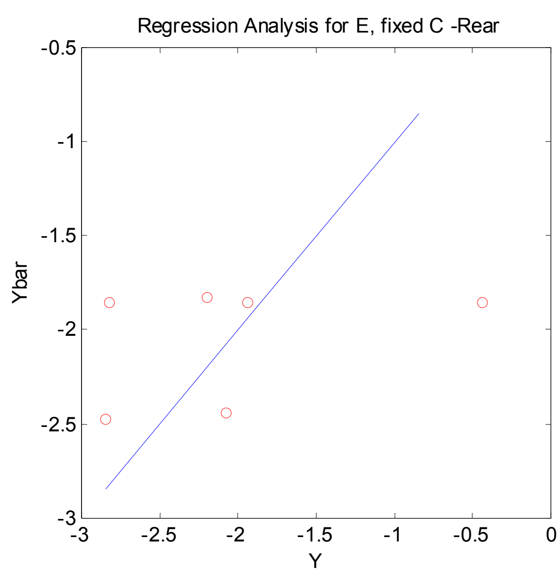

Fig. 3.33**: Regression analysis of E values for the rear wheel, with C fixed**

The values from the regression analysis have been compiled into a table shown in Fig. **3.34**. The *a* values show what effect each *x* variable had on the *y* variable, but, unfortunately the *a* values cannot be compared directly because they all have different units. It should be noted that while the tire thickness could be entered in the regression analysis in millimeters, it was not because the tires were not always constructed of one solid piece of rubber. There was only one size tire and for some test two of them were used on each wheel assembly. For this reason, the *x1* variable was either one or two, depending on the number of plies. The *x2* variable was the difference between the radius of the tire and the radius of the supporting metal wheel plate. The *x3* variable is the treadmill speed in meters per second. The *a1*, *a2*, and *a3* variables correspond to the *x1*, *x2*, and *x3* variables. As the regression analysis graphs show, the data is definitely statistically significant. Most of the points lie very close to the line, if they were all on it would indicate a perfect correlation between the changes in the variables and the corresponding *y* values.

Fig. **3.34**

Regression Analysis				
	Y	**a1 (# tire plies)**	**a2 (sidewall thickness mm)**	**a3 (speed m/s)**
	Cαf	-469.7782	8.6787	-11.175
	Cαr	-204.0912	3.5742	2.713
Front	B (with fixed C)	-23.6651	0.4223	-0.6628
	D (with fixed C)	15.16	-0.0758	0.1687
	E (with fixed C)	-6.6588	-0.4629	3.0009
Rear	B (with fixed C)	-16.2118	0.2514	0.1323
	D (with fixed C)	10.1762	-0.0248	-0.2902
	E (with fixed C)	-1.509	-0.0023	-0.31

Fig. 3.34**: Regression analysis a-values**

1. Wong, J.Y., *Theory of Ground Vehicles*. 3rd ed. 2001, New York: John Wiley & Sons, Inc.
2. Pacejka, H.B., *Tire and Vehicle Dynamics*. 2nd ed. 2006, Warrendale: SAE International.
3. Murray, G., *Magic Tire Model Plots: Cornering Stiffness Experiment*, The Pennsylvania State University.

Chapter 4
Conclusions and Recommendations

The most important thing gained from these experiments is that cornering stiffness can be commanded when designing solid rubber tires. This control is not infinite, but throughout the course of the experiments the cornering stiffness was increased by about 50% by simple changes in the tire design. This change can be attributed to certain factors controlled by the experimenter.

The three variables examined in these experiments were tire width, tire sidewall, and treadmill speed. Of these three, two of them dealt directly with tire construction; tire width and tire sidewall. The treadmill speed was varied to see if it would have any effect on the cornering stiffness. In theory, it should not. The speed did, however, have some effect on the cornering stiffness. As speed increased, so did cornering stiffness. This can probably be attributed to relatively low speed at which the treadmill was being run for many of the tests. In the future tests might be run at a higher speed.

The cornering stiffness also increased with decreasing sidewall length (Fig. **4.1**).

Fig. **4.1**

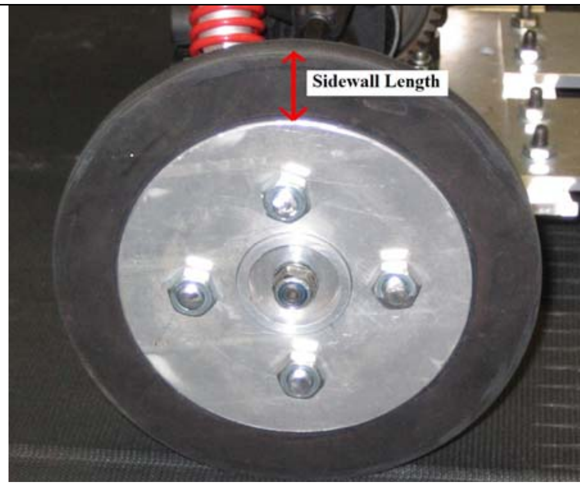

Fig. 4.1**: Sidewall Length of the tires on the scale vehicle**

This was as expected. The sidewall length was decreased during the test from 15.925 mm to only 2.9mm. This change alone accounts for about a 40-50% increase in sidewall stiffness. This means that an experimenter can have a large range of control over cornering stiffness solely by changing the sidewall diameter. Unfortunately this control is definitely limited. The final 2.9 mm sidewall length cannot be decreased for fear of the metal plates contacting the treadmill. If less cornering stiffness is needed, sidewall length could certainly be increased from the initial 15.925 mm length to give a larger range of cornering stiffness.

Increasing tire width was also found to increase the cornering stiffness. Doubling the effective width of the tire by using two tires at each corner instead of one increased the cornering stiffness by about 15%. With different hubs and longer bolts even wider tires could certainly be used. With a different thickness of rubber it would also be possible to vary the thickness of the tire over a much larger range of values. More testing could be used on the effect of different tire thicknesses. Another factor which was not examined was the use of different rubber compounds. In the future further testing could include other types of rubber if a larger range of cornering stiffness is needed.

The ability to "build" scale tires with a specific cornering stiffness is a great step forward. This will allow tires to be built to match the handling characteristics of real tires. The roadway simulator can then be used to test these scale vehicles and the data will be applicable for full-size vehicles.

Appendix A

Spreadsheet used to calculate slip angle and cornering stiffness from measured data (yaw angle, roll angle, steering motor angle)

	A	B	C	D	E	F	G	H	I	J	K	L	M
1	mass of car (kg)	a (front) (meters)	b (rear) (meters)	l (length of car)(m)	treadmill speed (m/s)								
2	11.4	0.24	0.415	0.655	1								
3													
4	TEST DATA	TEST DATA	TEST DATA	CALCULATED	CALCULATED	CALCULATED	CALCULATED	CALCULATED	PASTE special from sheet2	CALCULATED	CALCULATED	CALCULATED	CALCULATED
5	Treadmill Roll (deg)	Steering Motor Angle (rad)	Yaw Angle (deg)	Fy (N) (front tire)	Fy (N) (rear tire)	Steering Motor Angle Corrected (rad)	Yaw Angle Corrected (Deg)	Yaw Angle (rad)	corrected front wheel angle (rad)	Slip Angle Front (rad)	Slip Angle Front (deg)	Slip Angle Rear (rad)	Slip Angle Rear (deg)
6	-22.5	0.67	-5	13.56	7.84	0.61	-4.2	-0.0733	0.019095955	-0.0542	-3.11	-0.0733	-4.2
7	-20	0.6	-4.24	12.12	7.01	0.54	-3.44	-0.0600	0.016873908	-0.0432	-2.47	-0.0600	-3.44
8	-17.5	0.54	-3.6	10.65	6.16	0.48	-2.8	-0.0489	0.014975811	-0.0339	-1.94	-0.0489	-2.8
9	-15	0.47	-3.1	9.17	5.30	0.41	-2.3	-0.0401	0.012768876	-0.0274	-1.57	-0.0401	-2.3
10	-12.5	0.4	-2.65	7.67	4.43	0.34	-1.85	-0.0323	0.010569935	-0.0217	-1.24	-0.0323	-1.85
11	-10	0.35	-2.27	6.15	3.56	0.29	-1.47	-0.0257	0.009004104	-0.0167	-0.95	-0.0257	-1.47
12	-7.5	0.31	-1.98	4.62	2.67	0.25	-1.18	-0.0206	0.007754318	-0.0128	-0.74	-0.0206	-1.18
13	-5	0.21	-1.5	3.09	1.79	0.15	-0.7	-0.0122	0.004640922	-0.0076	-0.43	-0.0122	-0.7
14	-2.5	0.19	-1.22	1.55	0.89	0.13	-0.42	-0.0073	0.004020124	-0.0033	-0.19	-0.0073	-0.42
15	0	0.06	-0.8	0.00	0.00	0	0	0.0000	0	0.0000	0.00	0.0000	0
16	2.5	0.12	-0.53	-1.55	-0.89	0.06	0.27	0.0047	0.001852213	0.0066	0.38	0.0047	0.27
17	5	0.08	-0.2	-3.09	-1.79	0.02	0.6	0.0105	0.000616793	0.0111	0.64	0.0105	0.6
18	7.5	0.03	0.2	-4.62	-2.67	-0.03	1	0.0175	-0.00092405	0.0165	0.95	0.0175	1
19	10	-0.05	0.5	-6.15	-3.56	-0.11	1.3	0.0227	-0.00338154	0.0193	1.11	0.0227	1.3
20	12.5	-0.12	0.9	-7.67	-4.43	-0.18	1.7	0.0297	-0.005523999	0.0241	1.38	0.0297	1.7
21	15	-0.17	1.23	-9.17	-5.30	-0.23	2.03	0.0354	-0.007049893	0.0284	1.63	0.0354	2.03
22	17.5	-0.24	1.65	-10.65	-6.16	-0.3	2.45	0.0428	-0.00918	0.0336	1.92	0.0428	2.45
23	20	-0.32	2.17	-12.12	-7.01	-0.38	2.97	0.0518	-0.011605726	0.0402	2.31	0.0518	2.97
24	22.5	-0.39	2.8	-13.56	-7.84	-0.45	3.6	0.0628	-0.013720729	0.0491	2.81	0.0628	3.6

Spreadsheet used to calculate steering angle of the front wheels from the steering motor angle

	A	B	C	D	E	F	G	H	I
1	steering motor angle (rad) (F2	conversion (m/rad)	displacement (m)	a	b	c	beta (angle at wheels in rad)	corrected wheel angle (rad)	corrected wheel angle (deg)
2	0.61	0.00202163	0.0012332	0.1062	0.0656	0.1238	1.031564461	0.019095955	1.094117602
3	0.54	0.00202163	0.00109168	0.1061	0.0656	0.1238	1.029342415	0.016873908	0.966803719
4	0.48	0.00202163	0.00097038	0.106	0.0656	0.1238	1.027444317	0.014975811	0.858050771
5	0.41	0.00202163	0.00082887	0.1058	0.0656	0.1238	1.025237382	0.012768876	0.731602681
6	0.34	0.00202163	0.00068735	0.1057	0.0656	0.1238	1.023038441	0.010569935	0.605612663
7	0.29	0.00202163	0.00058627	0.1056	0.0656	0.1238	1.021472611	0.009004104	0.515897168
8	0.25	0.00202163	0.00050541	0.1055	0.0656	0.1238	1.020222824	0.007754318	0.444289668
9	0.15	0.00202163	0.00030324	0.1053	0.0656	0.1238	1.017109428	0.004640922	0.265905246
10	0.13	0.00202163	0.00026281	0.1053	0.0656	0.1238	1.01648863	0.004020124	0.230336116
11	0	0.00202163	0	0.105	0.0656	0.1238	1.012468506	0	0
12	0.06	0.00202163	0.0001213	0.1051	0.0656	0.1238	1.014320719	0.001852213	0.106123991
13	0.02	0.00202163	4.0433E-05	0.105	0.0656	0.1238	1.0130853	0.000616793	0.035339645
14	-0.03	0.00202163	-6.065E-05	0.1049	0.0656	0.1238	1.011544457	-0.00092405	-0.052944138
15	-0.11	0.00202163	-0.0002224	0.1048	0.0656	0.1238	1.009086966	-0.00338154	-0.19374799
16	-0.18	0.00202163	-0.0003639	0.1046	0.0656	0.1238	1.006944507	-0.005523999	-0.316501835
17	-0.23	0.00202163	-0.000465	0.1045	0.0656	0.1238	1.005418614	-0.007049893	-0.403929092
18	-0.3	0.00202163	-0.0006065	0.1044	0.0656	0.1238	1.003288507	-0.00918	-0.525975239
19	-0.38	0.00202163	-0.0007682	0.1042	0.0656	0.1238	1.000862781	-0.011605726	-0.664959098
20	-0.45	0.00202163	-0.0009097	0.1041	0.0656	0.1238	0.998747778	-0.013720729	-0.786139838

Spreadsheet of raw data recorded during all tests

	A	B	C	D	E	F	G	H	I	J	K	L	M	N	O
1															
2		Test 2		Test 3		Test 4		Test 5		Test 6		Test 7		Test 8	
3	Treadmill Roll (deg)	Steering Motor Angle (rad)	Yaw Angle (deg)	Steering Motor Angle (rad)	Yaw Angle (deg)	Steering Motor Angle (rad)	Yaw Angle (deg)	Steering Motor Angle (rad)	Yaw Angle (deg)	Steering Motor Angle (rad)	Yaw Angle (deg)	Steering Motor Angle (rad)	Yaw Angle (deg)	Steering Motor Angle (rad)	Yaw Angle (deg)
4	-25			1.34	-4.25	1.75	-7	1.8	-3.55	1.95	-3.25	1.67	-3.69	1.39	-6.32
5	-22.5	0.67	-5	1.31	-3.6	1.74	-4	1.77	-3.25	1.93	-2.86	1.62	-3.46	1.3	-5.97
6	-20	0.6	-4.24	1.25	-2.85	1.69	-2.45	1.72	-2.9	1.86	-2.6	1.59	-3.07	1.21	-5.25
7	-17.5	0.54	-3.6	1.22	-2.33	1.64	-1.85	1.66	-2.59	1.84	-2.32	1.56	-2.75	1.14	-4.72
8	-15	0.47	-3.1	1.15	-1.7	1.55	-1.3	1.65	-2.35	1.78	-2.21	1.5	-2.4	1.09	-4.22
9	-12.5	0.4	-2.65	1.08	-1.2	1.46	-0.8	1.61	-2.02	1.75	-1.72	1.42	-2.09	1	-3.9
10	-10	0.35	-2.27	0.99	-0.75	1.37	-0.45	1.56	-1.8	1.71	-1.61	1.4	-1.85	0.92	-3.6
11	-7.5	0.31	-1.98	0.9	-0.3	1.29	-0.08	1.51	-1.47	1.61	-1.35	1.36	-1.5	0.83	-3.2
12	-5	0.21	-1.5	0.82	0.1	1.21	0.3	1.46	-1.25	1.6	-1.13	1.24	-1.3	0.76	-2.9
13	-2.5	0.19	-1.22	0.73	0.55	1.1	0.7	1.42	-0.95	1.55	-0.79	1.17	-1.08	0.69	-2.55
14	0	0.06	-0.8	0.63	0.95	1.01	1.1	1.37	-0.7	1.51	-0.5	1.18	-0.85	0.63	-2.16
15	2.5	0.12	-0.53	0.54	1.4	0.94	1.64	1.32	-0.42	1.45	-0.25	1.18	-0.3	0.53	-1.84
16	5	0.08	-0.2	0.47	1.8	0.88	1.96	1.27	-0.18	1.43	-0.02	1.18	-0.15	0.47	-1.52
17	7.5	0.03	0.2	0.4	2.1	0.77	2.24	1.23	0.18	1.39	0.2	1.1	0.11	0.39	-1.17
18	10	-0.05	0.5	0.3	2.55	0.7	2.72	1.19	0.42	1.32	0.53	1.08	0.4	0.36	-0.72
19	12.5	-0.12	0.9	0.24	2.98	0.63	3.1	1.13	0.85	1.26	0.78	1.01	0.65	0.31	-0.31
20	15	-0.17	1.23	0.23	3.35	0.55	3.55	1.11	1.12	1.23	1.09	0.98	0.95	0.28	-0.21
21	17.5	-0.24	1.65	0.25	3.89	0.47	3.98	1.07	1.45	1.19	1.59	0.89	1.25	0.21	0.63
22	20	-0.32	2.17	0.2	4.4	0.38	4.55	1.05	1.9	1.17	2.05	0.87	1.65	0.17	1.14
23	22.5	-0.39	2.8	0.2	5.2	0.3	5.1	1.03	2.25	1.12	2.3	0.84	2.01	0.17	1.74
24	25			0.12	5.82	0.19	5.6	1	2.8	1.05	2.75	0.82	2.48	0.18	2.31

Spreadsheet of calculated slip angles and lateral forces from all tests

	A	B	C	D	E	F	G	H	I	J	K	L	M	N	O	P
1			Test 2		Test3		Test4		Test 5		Test 6		Test 7		Test 8	
2	Fy (N) (front tire)	Fy (N) (rear tire)	Slip Angle Front (Rad)	Slip Angle Rear (Rad)	Slip Angle Front (Rad)	Slip Angle Rear (Rad)	Slip Angle Front (Rad)	Slip Angle Rear (Rad)	Slip Angle Front (Rad)	Slip Angle Rear (Rad)	Slip Angle Front (Rad)	Slip Angle Rear (Rad)	Slip Angle Front (Rad)	Slip Angle Rear (Rad)	Slip Angle Front (Rad)	Slip Angle Rear (Rad)
3	14.97	8.66			-0.0685	-0.0908	-0.1181	-0.1414	-0.0363	-0.0497	-0.0343	-0.0480	-0.0343	-0.0496	-0.0487	-0.0726
4	13.56	7.84	-0.0542	-0.0733	-0.0581	-0.0794	-0.0661	-0.0890	-0.0321	-0.0445	-0.0281	-0.0412	-0.0318	-0.0456	-0.0455	-0.0665
5	12.12	7.01	-0.0432	-0.0600	-0.0469	-0.0663	-0.0406	-0.0620	-0.0275	-0.0384	-0.0258	-0.0367	-0.0260	-0.0387	-0.0358	-0.0539
6	10.65	6.16	-0.0339	-0.0489	-0.0388	-0.0572	-0.0318	-0.0515	-0.0240	-0.0330	-0.0215	-0.0318	-0.0213	-0.0332	-0.0288	-0.0447
7	9.17	5.30	-0.0274	-0.0401	-0.0300	-0.0463	-0.0250	-0.0419	-0.0201	-0.0288	-0.0215	-0.0298	-0.0171	-0.0271	-0.0216	-0.0360
8	7.67	4.43	-0.0217	-0.0323	-0.0235	-0.0375	-0.0191	-0.0332	-0.0156	-0.0230	-0.0139	-0.0213	-0.0142	-0.0216	-0.0189	-0.0304
9	6.15	3.56	-0.0167	-0.0257	-0.0185	-0.0297	-0.0159	-0.0271	-0.0133	-0.0192	-0.0132	-0.0194	-0.0106	-0.0175	-0.0161	-0.0251
10	4.62	2.67	-0.0128	-0.0206	-0.0134	-0.0218	-0.0119	-0.0206	-0.0091	-0.0134	-0.0117	-0.0148	-0.0058	-0.0113	-0.0120	-0.0182
11	3.09	1.79	-0.0076	-0.0122	-0.0090	-0.0148	-0.0078	-0.0140	-0.0068	-0.0096	-0.0082	-0.0110	-0.0060	-0.0079	-0.0089	-0.0129
12	1.55	0.89	-0.0033	-0.0073	-0.0039	-0.0070	-0.0042	-0.0070	-0.0028	-0.0044	-0.0038	-0.0051	-0.0043	-0.0040	-0.0050	-0.0068
13	0.00	0.00	0.0000	0.0000	0.0000	0.0000	0.0000	0.0000	0.0000	0.0000	0.0000	0.0000	0.0000	0.0000	0.0000	0.0000
14	-1.55	-0.89	0.0066	0.0047	0.0051	0.0079	0.0073	0.0094	0.0033	0.0049	0.0025	0.0044	0.0096	0.0096	0.0025	0.0056
15	-3.09	-1.79	0.0111	0.0105	0.0099	0.0148	0.0110	0.0150	0.0060	0.0091	0.0059	0.0084	0.0122	0.0122	0.0063	0.0112
16	-4.62	-2.67	0.0165	0.0175	0.0130	0.0201	0.0125	0.0199	0.0111	0.0154	0.0085	0.0122	0.0143	0.0168	0.0099	0.0173
17	-6.15	-3.56	0.0193	0.0227	0.0178	0.0279	0.0188	0.0283	0.0140	0.0195	0.0121	0.0180	0.0187	0.0218	0.0169	0.0251
18	-7.67	-4.43	0.0241	0.0297	0.0235	0.0354	0.0233	0.0349	0.0197	0.0271	0.0147	0.0223	0.0210	0.0262	0.0225	0.0323
19	-9.17	-5.30	0.0284	0.0354	0.0297	0.0419	0.0287	0.0428	0.0238	0.0318	0.0192	0.0278	0.0253	0.0314	0.0233	0.0340
20	-10.65	-6.16	0.0336	0.0428	0.0397	0.0513	0.0338	0.0503	0.0283	0.0375	0.0267	0.0365	0.0278	0.0367	0.0359	0.0487
21	-12.12	-7.01	0.0402	0.0518	0.0471	0.0602	0.0411	0.0602	0.0356	0.0454	0.0341	0.0445	0.0341	0.0436	0.0436	0.0576
22	-13.56	-7.84	0.0491	0.0628	0.0611	0.0742	0.0483	0.0698	0.0411	0.0515	0.0370	0.0489	0.0395	0.0499	0.0540	0.0681
23	-14.97	-8.66			0.0695	0.0850	0.0538	0.0785	0.0498	0.0611	0.0427	0.0567	0.0471	0.0581	0.0643	0.0780

Appendix B

Penn State Rolling Roadway Simulator

Design and Simulitude Validation of the Pennsylvania State University Rolling Roadway Simulator: the PURRS

Vishisht Gupta, Empar Callejas and Sean Brennan

Abstract— **This paper presents details on the design, dynamics, control, and similitude validation of a scale-sized vehicle and rolling-roadway simulator system: the Penn State University Rolling Roadway Simulator (PURRS). Among the unique features of the PURRS system are: 1) its utility in testing vehicle transient behavior during large lateral accelerations and/or vehicle roll angles; 2) the scale-sized vehicle can move freely in roll and pitch directions, thus allowing rollover studies to be conducted; and 3) the tires can be made to operate steadily near saturation to exhibit non-linear tire behavior. Design issues relating to the test-bed are presented in detail including system architecture and design of unique system components. This work also discusses model- and parameter-based matching of behavior of the scaled vehicle to a full-sized vehicle for dynamic similitude. Experiments are presented confirming the match of dynamic response of a full-sized vehicle to a dynamically similar scale-sized vehicle under similar excitations and control strategies.**

I. INTRODUCTION

Academic research in the field of vehicle chassis dynamics is often limited to simulation because the use of full-sized experimental vehicles is expensive as well as dangerous. The same problem exists in aerospace industry where wind-tunnels are commonly used with reduced scale experimental aircraft to test and validate initial designs. The goal of this research is to develop and validate a parallel concept to a wind-tunnel: a reduced-scale system concept for vehicles whereby a reduced scale version of the vehicle is driven on a rolling roadway for safe, easy and economic studies of vehicle dynamics and control particularly for rollover-inducing or tire-saturating conditions.

For high speed (highway speed) testing, one would like the vehicle to remain stationary with respect to the inertial frame and let the simulated road surface move relative to the vehicle. These types of systems are known as Rolling Roadway Simulators (RRS). While the number and usage of such systems has increased in recent years, these full-sized RRS [1]–[3] remain far too expensive for academic research.

There has been extensive use of reduced-scaled systems in the past to study the dynamics of all types of moving vehicles [4], [5] with the most famous example being the original work of the Wright Brothers (cite). Some previous investigations specifically using reduced-scale road vehicles [6]–[15], involved moving the vehicle along fixed roadway. This doesn't allow for simplification in terms of interfacing and sensing in comparison to experiments on full-sized vehicles. The first reduced-scale versions of a RRS were first developed by Brennan and others at Univ. of Illinois, Urbana-Champaign [22]–[25]. Similar systems are now used at United States Naval Academy (USNA) [19] and at Auburn University [20].

Just as early wind-tunnels focused mainly on lift effects while ignoring roll of the wing, most of the above scale-sized RRS examples strongly focus on lateral and yaw dynamics of the vehicle while largely neglecting roll dynamics and limit handling issues. The PURRS system at Pennsylvania State University was built to address such issues. The reduced-scale vehicle can move freely in roll and pitch directions, thus allowing coupling between lateral, yaw, and roll motion of the vehicle and facilitating rollover studies. The RRS also allows for controlled movement of the roadway itself in roll and pitch directions. The roll motion makes it possible to simulate turning maneuvers by tilting the roadway to induce a lateral acceleration. The large roadway roll angles available from this system can induce high lateral accelerations on the vehicle, leading to tire saturation and allowing study of the effects of nonlinear tire behavior on vehicle dynamics at the limits of performance. The roadway pitch motion facilitates testing of vehicles because the large pitch allows gravitationally-induced forward rolling of the vehicle. This allows vehicle testing without the need to install bulky drive motors because the pitch of the roadway can be servoed to maintain both the speed and position of the freely moving vehicle.

The work herin details the system setup, architecture unique to this system, as well as the similitude of the vehicle to full-size counterpart. In regard to this last point, whenever a scale-sized representation is used, caution must be exercised to ensure the matching of the dynamic response of a scaled vehicle to a dynamically similar full-sized vehicle under similar excitations and control strategies. Some previous research on scale-sized RRS have established dimensional transformations and pi-parameter matching to compare scale to full-size vehicles. Others have relied on input-output arguments to claim matching behavior (ref). The literature is devoid of an example where the reduced-scale vehicle is designed to match, and compared side-by-side to, a full-size vehicle counterpart using pi-parameter matching confirmed by input-output vehicle responses. This

Vishisht Gupta is a student in the department of Mechanical and Nuclear Engineering, Pennsylvania State University, University Park, PA vvg102@psu.edu

Empar Callejas is an exchange student in the department of Industrial Engineering, visiting Penn State 2004-05 from University of Barcelona, Spain.

Dr. Sean Brennan (corresponding author) is a faculty with the Department of Mechanical and Nuclear Engineering, Pennsylvania State University, University Park, PA snb10@engr.psu.edu

work is perhaps the first study in this area.

The paper is organized as follows: in section 2 the physical system design description is given. Section 3 describes the system dynamics in detail. An idealized bicycle model is presented and the various parameters for this model are derived using system identification. Section 4 verifies the model obtained in section 3 by presenting the data obtained from different experiments. Section 5 gives parameters for both a full-sized and a scale-sized vehicle to confirm dynamic similitude. A model for the full-sized vehicle has been determined independently by Cameron et al [27]. In Section 6 a comparison is performed between the dynamic responses from a full sized vehicle and a dynamically similar scaled vehicle. Conclusions then summarize the main points of the paper.

II. The Roadway Simulator: Overview and Sensing

The PURRS system consists of a 12'x7' treadmill and vehicle system (Fig. 1). The road belt velocity is controlled via a brush DC motor and is changed very slowly during normal testing to limit artificial longitudinal excitation induced on a vehicle by an accelerating roadway. The DC motor speed can be continuously varied using a speed controller giving the treadmill smooth velocity control up to a top speed of around 35 mph. The treadmill position in roll and pitch directions can be controlled. The maximum permissible angle in the roll direction is ($\pm 25°$) and in the pitch direction is ($\pm 6°$).

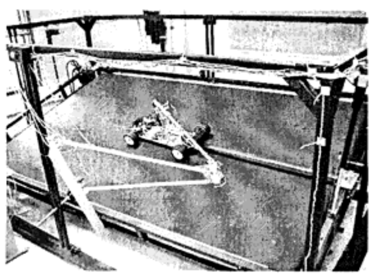

Fig. 1. The Roadway Simulator

The scaled vehicle currently used (Fig. 2)is approximately 1/5th length scaled. The chassis is equipped with a four bar steering mechanism, a double A suspension on front and rear wheels, and hydraulic brakes on all tires with two master cylinders. As most of the existing full-sized vehicles use hydraulic brakes, use of hydraulic brakes on the scaled system will result in a brake subsystem with similar dynamic response characteristics (delay, rise time) as an actual vehicle, and the dual system can be modified to allow different front vs rear braking control, or right versus left torque-inducing differential braking. The scaled vehicle also has a differential at the rear tires. Steering is achieved using a brushless DC motor (Pittman model 5441S006) whose bandwidth was carefully chosen and whose dynamics is discussed shortly.

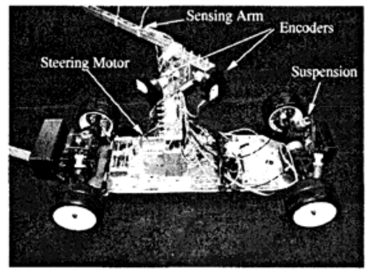

Fig. 2. Scaled vehicle

To implement various control algorithms on the scale-sized vehicle, the vehicle states must be measured or estimated. These include vehicle position, orientation and time derivatives of hese. To measure vehicle position and orientation, a sensing arm with five revolute joints is used. The sensing arm allows for free movement in roll and pitch directions, but these additional degrees of freedom complicate measurement of vehicle position and require transformations to resolve vehicle states from arm joint angles. Fig. 3 shows a kinematic representation of the sensing arm shown all available degrees of freedom. The arm has an optical encoder at each joint to measure each angle (US Digital Encoder model S2-2048-IB). Using these angles along with the fixed lengths of the arm, the position and orientation of the vehicle is calculated. The vehicle's position is obtained from the following equations:

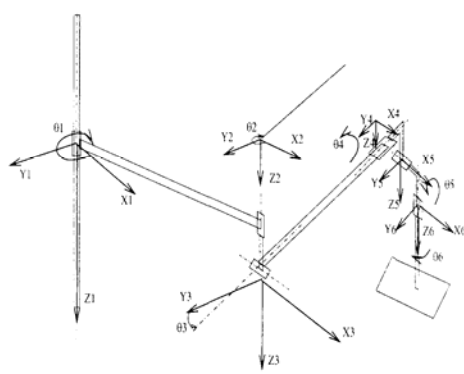

Fig. 3. Sensing Arm

Vishi, ground, encoders, and vehicle need to be labelled in the figure, and thetas and X's need to be subscripted.

$$X = L_1 \cos(\theta_1) + L_2 \cos(\theta_1 + \theta_2) \tag{1}$$

$$Y = L_1 \sin(\theta_1) + L_2 \sin(\theta_1 + \theta_2) \tag{2}$$

The calculation of roll and pitch is more involved. Fig. 3 shows a representation of the sensing arm 4 labelling all degrees of freedom. The following transformations give roll, pitch and yaw angles of the vehicle given the joint angles, θ_1 - θ_5. Here ${}^aT_b$ is the transformation from coordinate system C_b to coordinate system C_a. By multiplying all these transformations, the transformation from C_7 (car body coordinate system) to C_1 (earth-fixed coordinate system) is obtained. This transformation is exactly the same as the one obtained when the vehicle is rotated by Euler angles ϕ (roll), θ (pitch) and ψ (yaw), denoted here by $T_{\psi\theta\psi}$.

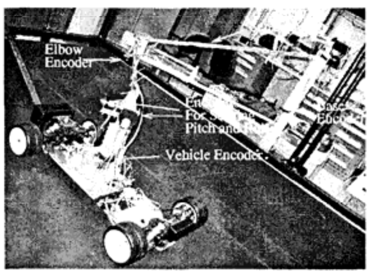

Fig. 4. Sensing Arm

$${}^1T_2 = \begin{pmatrix} \cos\theta_1 & -\sin\theta_1 & 0 \\ \sin\theta_1 & \cos\theta_1 & 0 \\ 0 & 0 & 1 \end{pmatrix} \tag{3}$$

$${}^2T_3 = \begin{pmatrix} \cos\theta_2 & -\sin\theta_2 & 0 \\ \sin\theta_2 & \cos\theta_2 & 0 \\ 0 & 0 & 1 \end{pmatrix} \tag{4}$$

$${}^3T_4 = \begin{pmatrix} 1 & 0 & 0 \\ 0 & \cos\theta_3 & -\sin\theta_3 \\ 0 & \sin\theta_3 & \cos\theta_3 \end{pmatrix} \tag{5}$$

$${}^4T_5 = \begin{pmatrix} \cos\theta_4 & 0 & -\sin\theta_4 \\ 0 & 1 & 0 \\ \sin\theta_4 & 0 & \cos\theta_4 \end{pmatrix} \tag{6}$$

$${}^5T_6 = \begin{pmatrix} 1 & 0 & 0 \\ 0 & \cos\theta_5 & -\sin\theta_5 \\ 0 & \sin\theta_5 & \cos\theta_5 \end{pmatrix} \tag{7}$$

$${}^6T_7 = \begin{pmatrix} \cos\theta_6 & -\sin\theta_6 & 0 \\ \sin\theta_6 & \cos\theta_6 & 0 \\ 0 & 0 & 1 \end{pmatrix} \tag{8}$$

$${}^1T_7 = {}^1T_2 \times {}^2T_3 \times {}^3T_4 \times {}^4T_5 \times {}^5T_6 \times {}^6T_7 \tag{9}$$

$${}^1T_7 = \begin{pmatrix} K_{11} & K_{12} & K_{13} \\ K_{21} & K_{22} & K_{23} \\ K_{31} & K_{32} & K_{33} \end{pmatrix} \tag{10}$$

$$T_{\psi\theta\phi} = \begin{pmatrix} C_\theta C_\psi & C_\theta S_\psi & -\sin_\theta \\ S_\phi S_\theta C_\psi - C_\phi S_\psi & S_\phi S_\theta S_\psi + C_\phi C_\psi & S_\phi C_\theta \\ C_\phi S_\theta C_\psi + S_\phi S_\psi & C_\phi S_\theta S_\psi - S_\phi C_\psi & C_\phi C_\theta \end{pmatrix} \tag{11}$$

By taking the ratio of different terms in the relation $T_{\psi\theta\phi} = {}^1T_7$, one obtains the values of roll, ϕ, pitch, θ, and yaw, ψ. By using terms (1,1) and (1,2), we get

$$\tan\psi = \frac{K_{12}}{K_{11}} \tag{12}$$

By using terms (2,3) and (3,3), we get

$$\tan\phi = \frac{K_{23}}{K_{33}} \tag{13}$$

By using (1,3), we get

$$\sin\theta = -K_{13} \tag{14}$$

These relationships will be used hereafter to control both vehicle position and treadmill speed as described below.

III. System Architecture and Control

There are numerous interacting control loops for vehicle and treadmill operation that require careful consideration of the system architecture. These include control loops for vehicle steering, treadmill velocity control, treadmill planar positioning, and longitudinal position control of the vehicle. Fig. 5 shows the simulator architecture. Control loops are implemented in a distributed, networked architecture using four Digital Signal Processors (DSPs) as controller and data-collection nodes. Actuators and sensors are interfaced to these DSPs using custom-made daughter cards. This distributed control scheme has many advantages over centralized control architecture used for other scaled RRS [22]–[25]. One, a single processor may not be able to process all the control functions in a given time period, particularly when advances sensing architectures are used such as computer vision. Second, a distributed control scheme can be used to provide sub-system isolation and redundancy so that the system can accommodate failure in some components. The DSPs communicate with each other using a controller area network (CAN) bus as used in automotive applications. CAN being a differential bus and therefore has significant inherent immunity to EMI and other noise including inherent error detection and confinement capabilities. Data rates up to 1Mbit/s are supported.

As shown in Fig. 5, one DSP (the "master") is solely dedicated to communication to the human user via connection to a PC via a parallel port. The PC is running a real-time windows-based program, Wincon (Quanser consulting), that provides plotting and data-logging features for code generated by MATLAB's real-time workshop. The interface loop operates at 200 Hz.

A. Treadmill Roll and Pitch Position Control System

For safety and redundancy, four linear actuators (Fig. 8) (HAVE TO CHANGE PICTURE TO BE ABLE TO SEE FOUR ACTUATORS) are used to tilt the treadmill in pitch and roll directions; however, coordination of these is challenging: only three linear actuators are necessary to form a plane. Thus, the fourth actuator must move in coordination so as to conform to the plane condition formed by the other three. This coordination must occur regardless of faults in actuators/sensors and the system should shut itself off when this coordination cannot be maintained.

To calculate the conditions necessary for a planar condition, the geometry of the physical system is considered. Figs. 6 and 7 depict the treadmill geometry in pitch and roll direction showing the treadmill at an initial and a final position after the treadmill has moved through an angle θ in the pitch direction and an angle ϕ in the roll direction. From the geometry of the problem, the following relations exist between different lengths as shown in Figs. 6 and 7.

From Fig. 6, assuming the pitch angle is small, we get the relation 15.

$$\Delta Z = L_T \sin\phi \tag{15}$$

$$L_{W1}^2 = Y_W^2 + Z_W^2 \tag{16}$$

$$\Delta Y_W = L_L(1-\cos\theta) \tag{17}$$

$$\Delta Z_W = L_L \sin\theta \tag{18}$$

$$L_{W2}^2 = (Y_W + \Delta Y_W)^2 + (Z_W + \Delta Z_W)^2 \tag{19}$$

$$Y_W = H_0 - \Delta Z \tag{20}$$

From Fig. 7, eqns. 16 gives the string potentiometer length before the treadmill rolls. Eqns. 17 and 18 calculate the change in length of the wire in Y and Z directions and eqn. 19 uses those to calculate the final wire length L_{W_2} after the treadmill rolls by and angle θ.

Here H_0 is the distance between the treadmill frame and the treadmill surface at the "home" position. As the maximum permissible angle in the pitch direction is small ($\pm 6°$), a small angle approximation has been used whereby $(\tan\theta = \sin\theta) = \theta$.

A system of four on/off relays is used to actuate the linear actuators to maintain the planar condition while at the same time achieving the desired roll and pitch angles of the roadway surface. String potentiometers are used for position feedback of the linear actuators. The actuators are severely rate limited. Depending on the commanded position, they all cannot be always moved in the desired direction simultaneously. The algorithm for keeping the four linear actuators in a plane is explained below which accounts for the geometry of the current and desired position as well as the rate limit of the actuators.

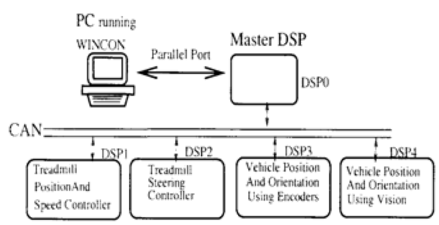

Fig. 5. Vehicle Test-bed Architecture

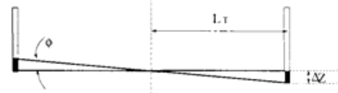

Fig. 6. Treadmill Geometry in the Pitch Direction

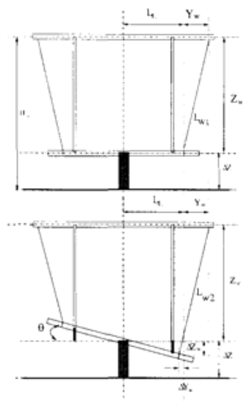

Fig. 7. Treadmill Geometry in the Roll Direction

The condition that the four actuators should form a plane is checked at every control time step. This condition, when simplified, is very simple: the center of the treadmill as calculated by averaging the two opposite corners of the treadmill should be the same regardless of which diagonal the averaging occurs. For example, the plane condition for the two positions of the treadmill is:

$$\Delta Z_1 + \Delta Z_3 = \Delta Z_2 + \Delta Z_4 \tag{21}$$

For any commanded reference position θ and ϕ, the final perturbed position of the linear actuators, can be calculated from the measured equations above and used in a feedback loop. This final position is compared to the present position of the actuators to determine their direction of motion. Bang-bang control is implemented using relays where the actuators are either ON or OFF. One of the actuators (Actuator 4 as implemented) is always moved so as to satisfy the plane condition. If the plane condition is

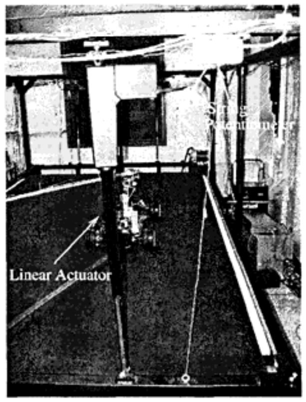

Fig. 8. Linear Actuator Used to Move the Test-bed

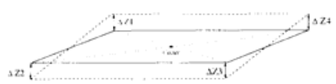

Fig. 9. Displacements of the four actuators from initial to final position

not satisfied at any time (within a specified tolerance), all the actuators except the one moving to satisfy the plane condition (actuator 4) are disabled and only enabled when the plane condition is satisfied again. If the final position is such that it is not possible to move all the actuators at the same time because of speed limit constraint, the actuators are given preference in the order 1, 2 and 3. This can be seen clearly by taking the derivative of the plane condition equation (21).

$$\frac{d\Delta Z_4}{dt} = \frac{d\Delta Z_1}{dt} + \frac{d\Delta Z_3}{dt} - \frac{d\Delta Z_2}{dt} \tag{22}$$

$$\left|\frac{d\Delta Z_4}{dt}\right| = \left|\frac{d\Delta Z_1}{dt}\right| = \left|\frac{d\Delta Z_3}{dt}\right| = \left|\frac{d\Delta Z_2}{dt}\right| = c(Const)$$

For all the possible situations where the absolute value of the right hand side of (22) is greater than $2 \cdot c$, it is not possible to move all the actuators at the same time. If the plane condition is violated by more than a pre-specified tolerance limit, the whole system is shut down. Fig. 10 shows a plot when the commanded position of the four actuators necessitated a sequential motion of the actuators. Notice that actuator 4 always moves so as to satisfy the plane condition and the other three actuators take turns to move so as to satisfy the rate limit condition.

IV. VEHICLE DYNAMICS

Vehicle dynamics has been simulated using two different vehicle models. One will be the 2DOF model assuming no

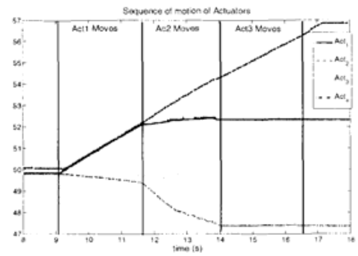

Fig. 10. Sequence of operation of the actuators

U_x	Longitudinal velocity at CG(body-fixed frame)
U_y	Lateral velocity at CG(body-fixed frame)
M	Vehicle mass
M_s	Vehicle sprung mass
I_{zz}	Inertia about the vertical (Z) axis
I_{xx}	Inertia about the roll (X) axis
l_f	Front axle to CG distance
l_r	Rear axle to CG distance
L	Track of vehicle ($l_f + l_r$)
T	Width of vehicle
K_f	Effective roll stiffness of the suspension
D_f	Effective roll damping of the suspension
h	CG height
α_f	Slip angle of the front tires
α_r	Slip angle of the rear tires
β	Slip angle of the vehicle body
C_f	Front cornering stiffness
C_r	Rear cornering stiffness
δ_f	Front steering angle

TABLE I
NOMENCLATURE

roll dynamics. This model commonly referred to as "bicycle model" assumes a single track vehicle with only two states, taking only lateral and yaw dynamics into account. Some application examples of this model can be found in [28]–[32]. This relatively simple model is used to get a number of vehicle parameters. The other model takes into account the roll dynamics of the vehicle. SAE sign convention has been followed while deriving these vehicle models.

A. Bicycle Model

The equations of motion for the bicycle model can be derived by balancing forces and moments on the vehicle as shown in Fig. 11. The equations in the state space form are

$$\begin{bmatrix} \dot{U}_y \\ \dot{r} \end{bmatrix} = \begin{bmatrix} \frac{-C_f - C_r}{mU} & \frac{C_r l_r - C_f l_f}{mU_x} - U_x \\ \frac{C_r l_r - C_f l_f}{I_{zz} U_x} & \frac{-C_f l_f^2 - C_r l_r^2}{I_{zz} U_x} \end{bmatrix} \begin{bmatrix} U_y \\ r \end{bmatrix} + \begin{bmatrix} \frac{C_f}{m} \\ \frac{C_f l_f}{I_{zz}} \end{bmatrix} \delta_f \tag{23}$$

B. 3DOF Model With Roll Dynamics

This model was derived in body-fixed coordinates and lateral velocity, yaw rate and roll rate were taken as vehicle states [33]. Various conventions and variables used in this model are given in Fig. 12.

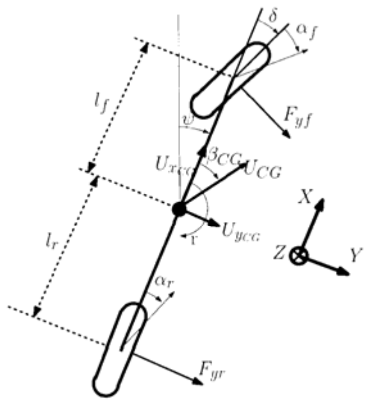

Fig. 11. Bicycle Model

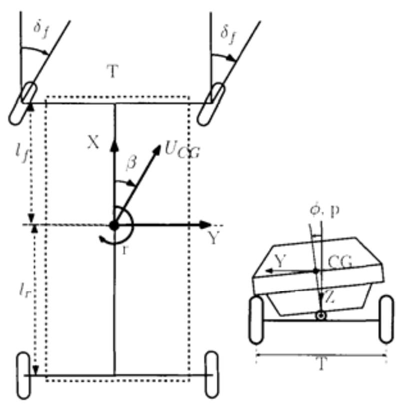

Fig. 12. Roll Model

The roll model in the state space form is

$$E\dot{x} = Ax + Bu + L\delta_f \tag{24}$$
$$y = Cx + Du \tag{25}$$

where

$$x = [U_y \quad r \quad \phi \quad p]^T \tag{26}$$

$$A = \begin{bmatrix} -\frac{(C_f+C_r)}{U_x} & \left(-MU_x - \frac{(C_r l_r - C_f l_f)}{U_x}\right) & 0 & 0 \\ \frac{(C_r l_r - C_f l_f)}{U_x} & -\frac{(C_f l_f^2 + C_r l_r^2)}{U_x} & 0 & 0 \\ 0 & 0 & 0 & 1 \\ 0 & -M_s h U_x & -K_f & -D_f \end{bmatrix} \tag{27}$$

$$B = [0 \quad 0 \quad 0 \quad 1]^T \tag{28}$$
$$L = [C_f \quad C_f l_f \quad 0 \quad 0] \tag{29}$$
$$C = [0 \quad 0 \quad 1 \quad 0] \tag{30}$$
$$D = 0 \tag{31}$$

$$E = \begin{bmatrix} M & 0 & 0 & M_s h \\ 0 & I_{zz} & 0 & 0 \\ 0 & 0 & 1 & 0 \\ M_s h & 0 & 0 & I_{xx} \end{bmatrix} \tag{32}$$

V. MATCHING TO FULL SIZED VEHICLE

The parameter values for the full-sized vehicle are taken from [27]. These values are given in Table II.

Variable	Value
M	1030 Kg
W_f	6339 Kg
W_r	3781 Kg
M_s	825 Kg
I_{zz}	1850 $Kg - m^2$
I_{xx}	375 $Kg - m^2$
l_f	0.93 m
l_r	1.56 m
T	1.4 m
h	0.52 m
K_ϕ	53000 $\frac{N}{rad}$
D_ϕ	7000 $N - s/rad$
C_f	45500 $\frac{N}{rad}$
C_r	76650 $\frac{N}{rad}$

TABLE II
PARAMETERS FOR MERCURY TRACER

TO ADD

- CORNERING STIFFNESS RESULTS.
- DYNAMIC SIMILITUDE BY PI PARAMETER MATCHING.
- EXPERIMENTS DONE TO MATCH PI PARAMETER VALUES.
- FREQUENCY RESPONSE TESTS AND MATCHING WITH FULL SCALE VEHICLE

VI. SCALE SIMILARITY

A. STEERING ACTUATOR DYNAMICS

In addition to matching the chassis behavior of the vehicle, the actuator dynamics were also matched. The PURRS vehicle steering actuator was designed to have a bandwidth of 15 Hz based on the observation that steer-by-wire actuator dynamics reported in literature (HAVE TO ADD REFERENCES) have a bandwidth of approximately 5 Hz. The scaling ratio of XXX was obtained by...

Fig. 13 shows the steering mechanism on the scaled vehicle which consists of a brushless DC motor driving a rack-and-pinion gear system with anti-backlash drive gears. The frequency response of the entire system was obtained for various amplitudes of excitation, and a second order model was matched to the measured data (Fig. 14). The transfer function from reference steering angle, δ_{Ref}, to output steering angle, δ_{Out}, is given below.

$$\frac{\delta_{Out}}{\delta_{Ref}} = \frac{120^2}{s^2 + 2 * 0.35 * 120 + 120^2} \tag{33}$$

It was found that this model was quite suitable for front wheel steering angles of $5°$ amplitude or less.

COMPARISON PLOTS BETWEEN MODEL AND ACTUAL RESPONSE WILL BE GIVEN IN TIME DOMAIN. WHILE DOING LATERAL CONTROL AND FREQUENCY RESPONSE EXPERIMENTS ON THE VEHICLE, THE AMPLITUDES REQUIRED FROM THE STEERING ACTUATORS WILL BE DETERMINED AND THEN THE STEERING RESPONSE WILL BE BETTER MATCHES FOR THAT AMPLITUDE.

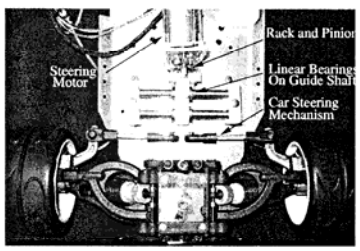

Fig. 13. Scaled vehicle steering system

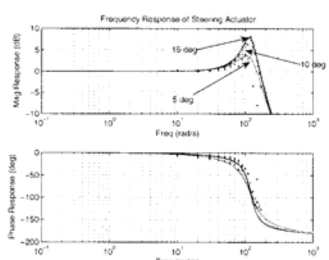

Fig. 14. Steering System Frequency Response

VII. CONCLUSION

Once the matching is established, the simulator will be used in the future to design and test advanced chassis control algorithms. These include, for example, control strategies to prevent rollover.

VIII. ACKNOWLEDGMENTS

Authors would like to thank Mike Schroeder for his assistance in construction of the treadmill.

REFERENCES

[1] W. Langer. Vehicle Testing With Flat surface Roadway Technology. Society of automotive Engineers Paper No. 960731, 1996.

[2] W. Langer. validation of Flat Surface Roadway Technology, society of Automotive Engineers Paper No. 950310, 1995.

[3] G. Schultz, Tong, I., Kefauver, K. and Ishibashi, J. (2005)"Steering and Handling Testing Using Roadway Simulator Technology", Int. J. of Vehicle Systems Modeling and Testing, Vol. x., No. x, pp. xxx-xxx.

[4] T.A. McMahon and J.T. Bonner, *On Size and Life*. New York: Scientific American, 1983.

[5] M.G. Bekker, *Introduction to Terrain-Vehicle Systems*. Ann Arbor, MI: Univ. of Michigan Press, 1969.

[6] N. Matsumoto and M. Tomizuka, "Vehicle Lateral Velocity and Yaw Rate Control with Two Independent Control Inputs", *in ASME JDSMC*, Vol. 114, 1992, pp 606-613.

[7] P. Kashroo, K. Ozbay, R.G. Leonhard and C. Unsal, "Flexible Low-cost Automated Scaled Highway (FLASH) Laboratory for Studies in Automated Highway Systems", *in Proceedings of IEEE Intl. Conf. on Systems, Man and Cybernetics*, Vancouver, Canada, 1995.

[8] M Sampei, T. Tamura, T. Kobayashi and N. shibui, "Arbitrary Path Tracking control of Articulated Vehicles Using Nonlinear Control Theory", *in IEEE Trans. on Control System Technology*, Vol. 3, No. 1, pp 125-131, March, 1995.

[9] A. Divelbiss, J.T. Wen, "Trajectory Tracking Control of a Car-Trailer System", *in IEEE Transaction on Control System Technology*, Vol. 5, No. 3, pp269-278, May, 1997.

[10] R. S. Woodley and L. Acar, "A Testbed System for Nonlinear or Intelligent Control", *in Proceedings of the 1999 American Control Conference*, San Diego, California, pp 3441-3445, June 1999.

[11] Philippe Martinet, Christian Thibaud, Benoit Thuilot, Jean Gallice , "Robust controller synthesis in automatic guided vehicles applications", *in Proceedings of the International Conference on Advances in Vehicle Control and Safety*, AVCS, pp 395-401, Amiens, France , 1-3 July 1998.

[12] Richard D. Henry, "Automatic Ultrasonic Headway control for a Scaled Robotic Car", *Master's Thesis, Virginia Polytechnic Institute and State University*, Blackburg, Virginia.December, 2001.

[13] G. Caprari, T. Estiera and R. Siegwart, "Fascination of Down Scaling Alice the Sugar Cube Robot", *Workshop on mobile micro-robots, ICRA'00*, pp 15-20, 2000.

[14] J. Gohl, R. Rajamani, L. Alexander and P. Starr, "The Development of Tilt-Controlled Narrow Ground Vehicles", *in Proceedings of American Control Conference*, Anchorage, AK, May, 2002.

[15] Robert Woodley and Levent Acar, "Autonomous Control of a Scale Model of a Trailer-Truck Using an Obstacle-Avoidance Path-Planning Hierarchy", *in American Control conference*, Boston, Massachusetts, June, 2004.

[16] S. Brennan, M. DePoorter, and A. Alleyne, "The Illinois Roadway Simulator - A Hardware-in-the-Loop Testbed for Vehicle Dynamics and Control", *in American Control Conference*, Philadelphia, PA, 1998.

[17] S. Brennan and A. Alleyne, "A Scaled Testbed for Vehicle Control: the IRS", *in IEEE International Conference on Control Applications*, Kohala Coast, Island of Hawaii, 1999.

[18] S. Brennan and A. Alleyne, "The Illinois Roadway Simulator: A Mechatronic Testbed for Vehicle Dynamics and Control", *in IEEE/ASME Transactions on Mechatronic Ssytems* , vol. 5, 2000.

[19] Richard T. OBrien.Jenelle A. Piepmeier, Philip C. Hoblet, Steven R. Burns, and Charles E. George, "Scale-Model Vehicle Analysis Using an Off-the-Shelf Scale-Model Testing Apparatus", *in American Control Conference*, Boston, Massachusetts, June, 2004.

[20] William E. Travis, Randy J. Whitehead, David M. Bevly, and George T. Flowers, "Using Scaled Vehicles to Investigate the Influence of Various Properties on Rollover Propensity", *in American Control Conference*, Boston, Massachusetts, June, 2004.

[21] M. S. Polley, "Size Effects on Steady State Pneumatic Tire Behavior: An Experimental Study", *Master's Thesis*, University of Illinois at Urbana-Champaign, 2001.

[22] S. Brennan and A. Alleyne, "Robust Scalable Vehicle Control via Non-Dimensional Vehicle Dynamics", *in Proceedings AVEC, 5th intl. Symposium on Advanced Vehicle Control*, Ann Arbor, Michigan, August, 2000.

[23] S. Brennan and A. Alleyne, "Integrated Vehicle Control Via Coordinated Steering and Wheel Torque Inputs", *in Proceedings of ACC*, Arlington, VA, June, 2001.

[24] S. Brennan and A. Alleyne, "Using a Scale Testbed: Controller Design and Evaluation", *IEEE Control System Magazine*, June 2001.

[25] S. Brennan and A. Alleyne, "H-infinity Vehicle Control Using NonDimensional Perturbation Measures", *in Proceedings of ACC*, Anchorage, AK, May, 2002.

[26] P. Martinet, C. Thibaud, D. Khadraoui and J. Gallice, "Robust Controller Synthesis in Automatic Guided Vehicles Applications", *in Proceedings of intl. Conference on Advances in Vehicle Control and Safety, AVCS'98*, pp. 395-401, Amiens, France, July, 1998.

[27] J. Cameron and S. Brennan, " A comparative, experimental study of model suitability to describe vehicle rollover dynamics for control design",*in Proceedings of Intl. Mechanical Engineering Congress and Exposition, IMECE*, Orlando, Florida, November, 2005.

[28] S. Saraf and M. Tomizuka, "Slip Angle Estimation for Vehicles on Automated Highways",*in Proceedings of the 1997 American Control Conference*, Albuquerque, New Mexico, 1997.

[29] D. M. Bevly, R. Sheridan, and J. C. Gerdes, "Integrating INS Sensors with GPS Velocity Measurements for Continuous Estimation of Vehicle Sideslip and Tire Cornering Stiffness",*in Proceedings of the 2001 American Control Conference*, Arlington, Virginia, 2001.

[30] J. Ackermann, W. Sienel, and R. Steinhauser, "Robust automatic steering of a bus",*presented at Proceedings of the Second European Control Conference (ECC)*, Groningen, The Netherlands, 1993.

[31] S. Mammar and V. B. Baghdassarian, "Two-degree-of-freedom Formulation of Vehicle Handling Improvement by Active Steering",*presented at Proceedings of the 2000 American Control Conference*, Chicago, Illinois, 2000.

[32] S.-S. You and S.-K. Jeong, "Controller design and analysis for automatic steering of passenger cars",*Mechatronics*, vol. 12, pp. 427–446, 2002.

[33] H. J. Kim and Y. P. Park, "Investigation of robust roll motion control considering varying speed and actuator dynamics",*Mechatronics*, 2003.

Appendix C

Magic Tire Model Plots: Cornering Stiffness Experiment by ***Gareth E. Murray Jr.***

$$F_y = D\sin(C\arctan(B\Phi)) + S_v$$
$$\Phi = (1 - E)(\alpha + S_h) + (E/B)\arctan(B(\alpha + S_h))$$
$$D = a_1 F_z^2 + a_2 F_z$$
$$C = 1.30$$
$$B = \left[\frac{a_3 \sin(a_4 \arctan(a_5 F_z))}{CD}\right]$$
$$E = a_6 F_z^2 + a_7 F_z + a_8$$

Magic Tire Model Plots: Cornering Stiffness Experiment

Below are the results of our magic tire model curve fitting for each experiment. These models allow us to characterize the behavior of tires for various conditions and provide the benefit of using an equation(s) to extract tire property data rather than an extensive experiment(s). Figures 1 – 4 show the results of the cornering stiffness experiment with the characterization model plotted on top of them for comparison (the models are solid lines, the experiment results are data points). Each equation can be "tweaked" for accuracy in matching the experimental data; the variables for these equations are noted on the plots. Figures 5 – 7 show how these variables, namely the curvature and shape factors E, B, and D, change with respect to the normal load on the tires. The results shown in Figures 1 - 7 give us a complete set of equations whereby all relevant properties of our first tire can be characterized and predicted for a variety of conditions. Figure 8 relates the cornering stiffness (C_alpha) to the normal load experienced on one rear tire.

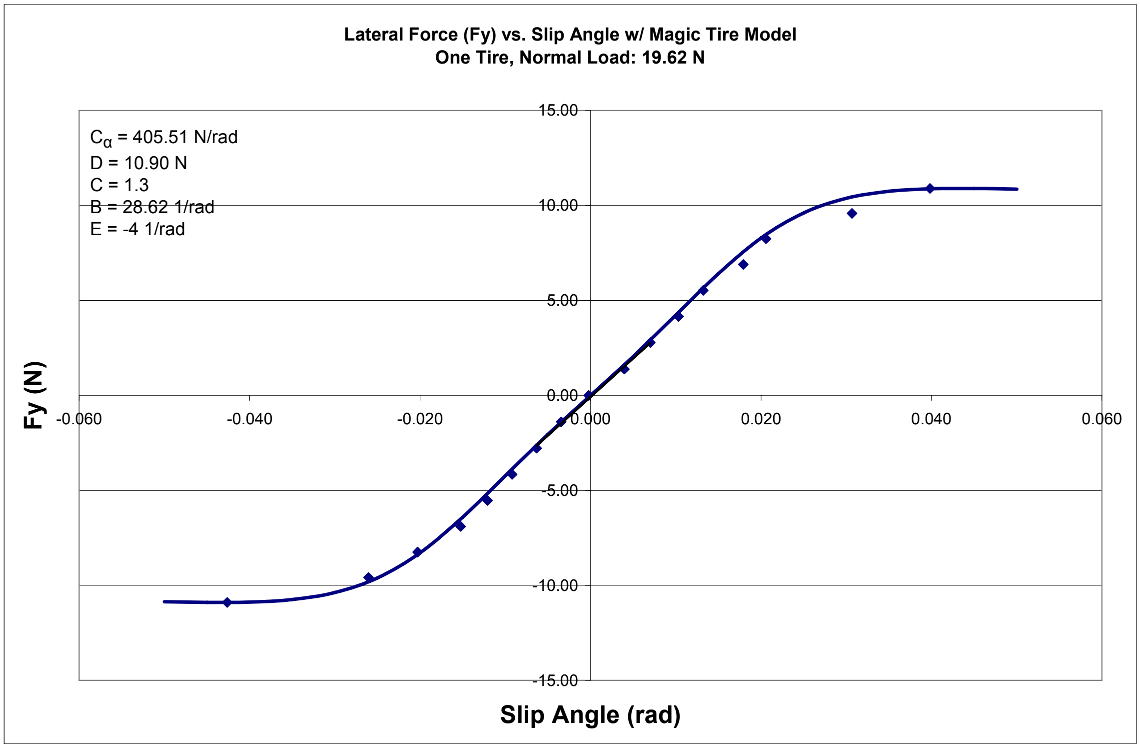

Figure 1. Lateral Force vs. Slip Angle for no applied load: Magic Tire Model Included

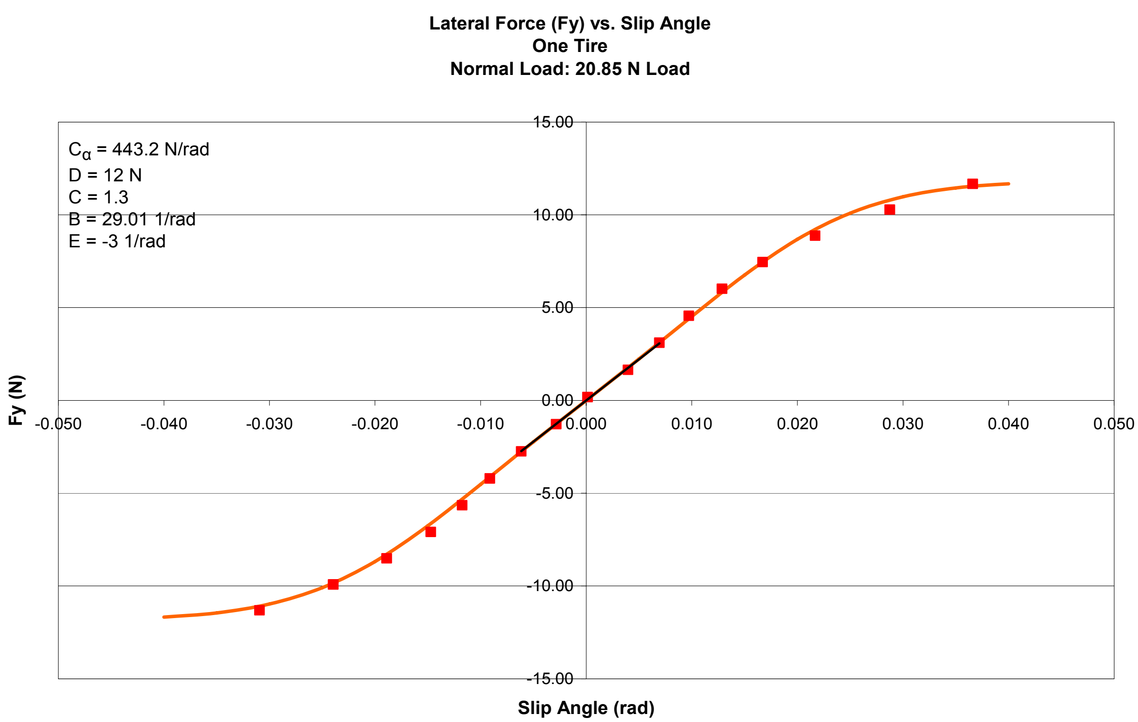

Figure 2. Lateral Force vs. Slip Angle for Load = 0.5kg: Magic Tire Model Included

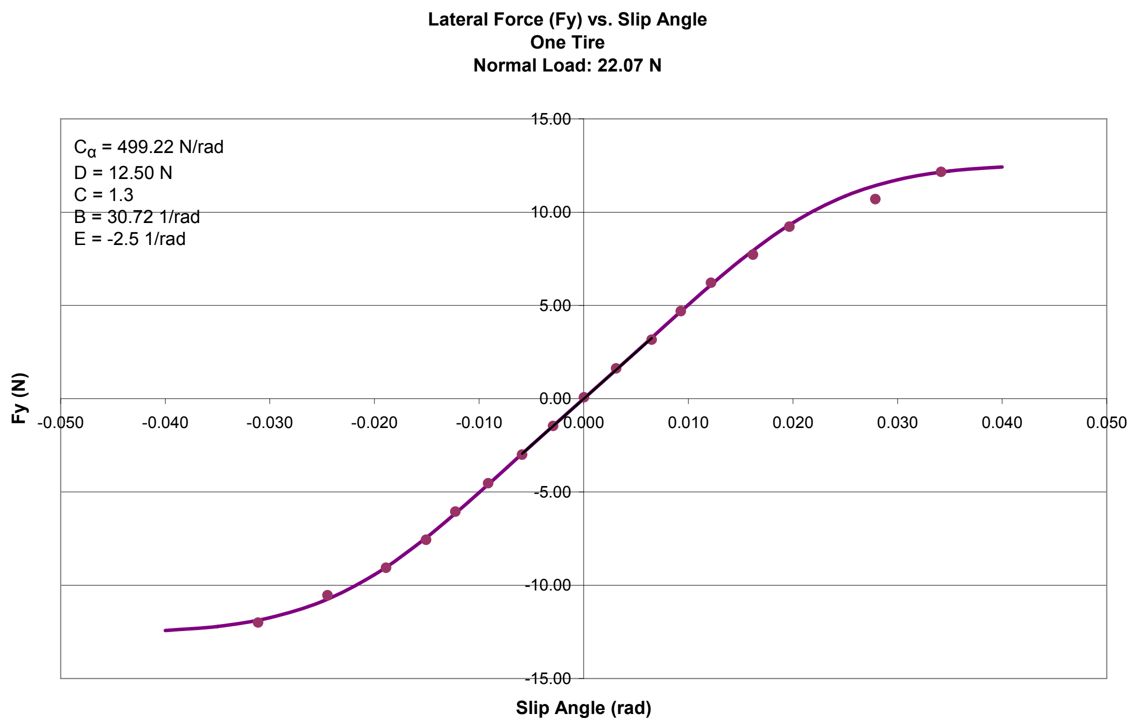

Figure 3. Lateral Force vs. Slip Angle for Load = 1.0kg: Magic Tire Model Included

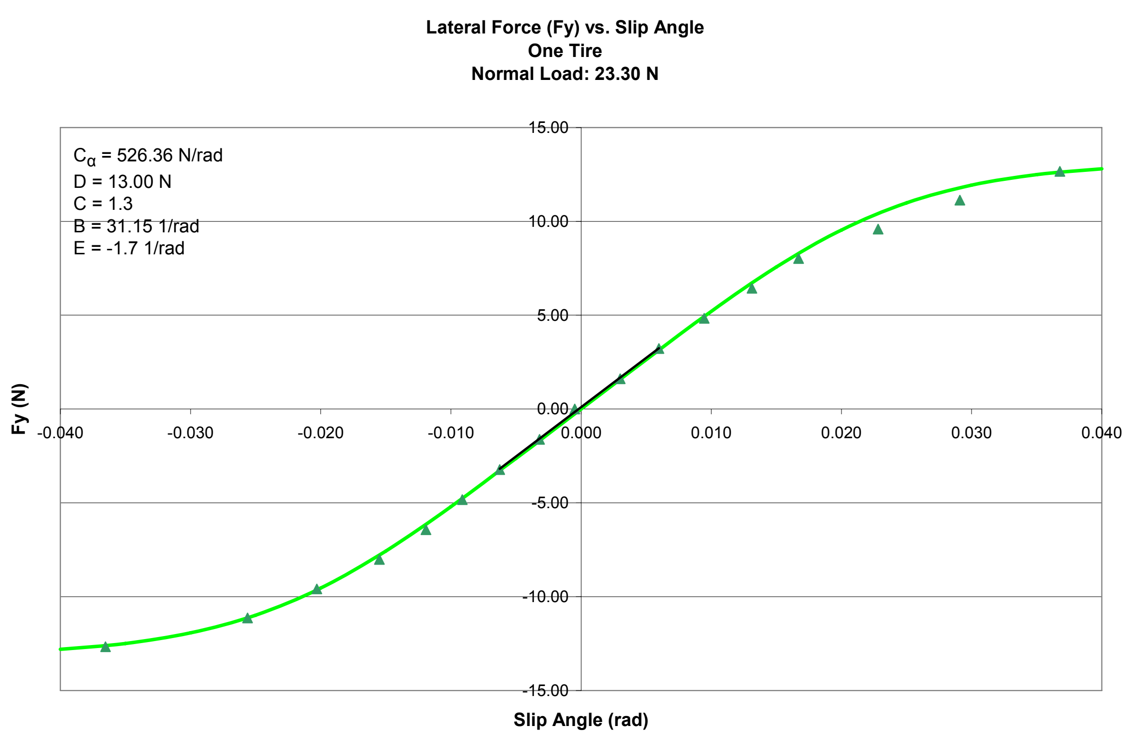

Figure 4. Lateral Force vs. Slip Angle for Load = 1.5kg: Magic Tire Model Included

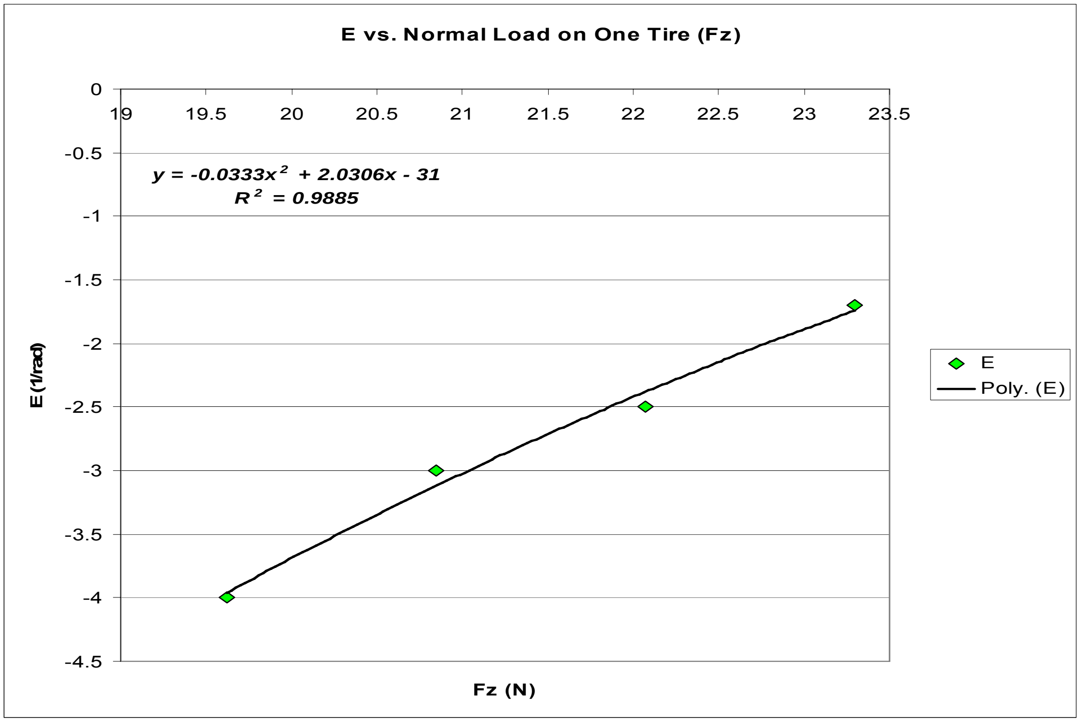

Figure 5. Plot of E vs. Normal Load on One Tire

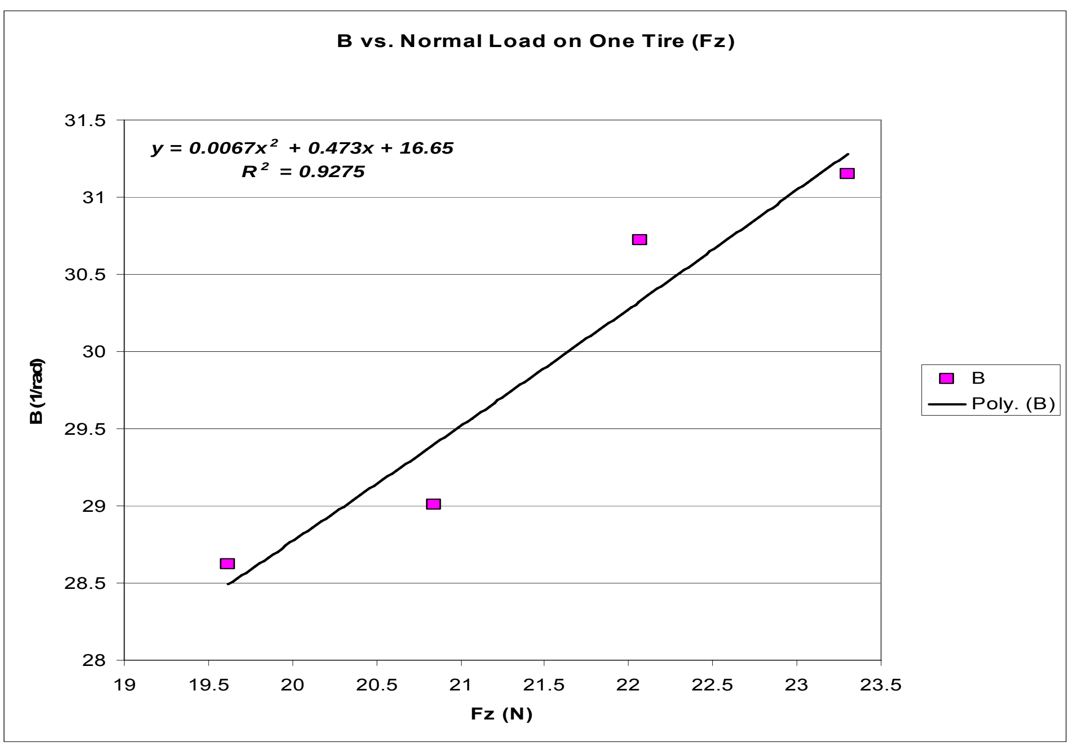

Figure 6. Plot of B vs. Normal Load on One Tire

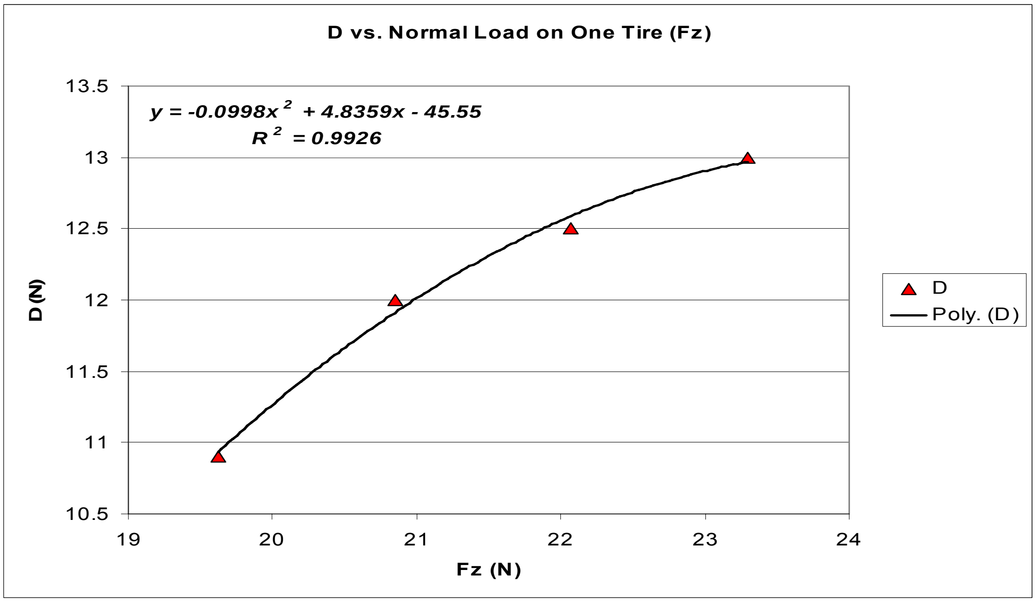

Figure 7. Plot of D vs. Normal Load on One Tire

The Magic Tire Model:

$$F_y = D\sin(C\arctan(B\Phi)) + S_v$$
$$\Phi = (1-E)(\alpha + S_h) + (E/B)\arctan(B(\alpha + S_h))$$
$$D = a_1 F_z^2 + a_2 F_z$$
$$C = 1.30$$
$$B = \left[\frac{a_3\sin(a_4\arctan(a_5 F_z))}{CD}\right]$$
$$E = a_6 F_z^2 + a_7 F_z + a_8$$

Solutions from plot results:

$D = -0.0998*F_z^2 + 4.8359*F_z - 45.55$ (R2 = 0.9926)

$C = 1.30$

$B = 0.0067*F_z^2 + 0.473*F_z + 16.65$ (R2 = 0.9275)

$E = -0.0333*F_z^2 + 2.0306*F_z - 31$ (R2 = 0.9885)

Sv = Sh = 0 (engineering assumption)